

A Lost in the space

“After the planned momentum management, while still in thruster mode, the Attitude and Orbit Control Subsystem (AOCS) switched into ESR (Emergency Sun Re-acquisition) mode on 24 June at 23:16, due to a procedure problem. On 25 June at 02:35 a second ESR occurred during standard ESR recovery, triggered by a roll rate anomaly; the reason is unclear. Some time later, at 04:38, a third ESR triggered by a fine Sun-pointing anomaly and all telemetry was lost.”

This message was issued by the SOHO Operations Team on 25 June 1998. The telemetry of the satellite had been lost and no communication was possible between ground controllers and the spacecraft. An ESA/NASA investigative board identified three separate causes for the accident. The first was a preprogrammed software sequence that lacked a command to turn on a gyroscope necessary to reorient SOHO toward the Sun in case of an emergency. A second faulty command sequence caused one of the spacecraft's three gyroscopes to return an incorrect reading. That reading sent SOHO into Emergency Sun Reacquisition (ESR) mode, which eventually failed. Finally, controllers on the ground, confused about which gyroscope was malfunctioning, sent SOHO a command to turn off a functioning gyroscope. These sequence of events apparently sent the spacecraft into a spin that misaligned its communications antenna and turned its solar panels away from the Sun. After three months of hard work by the recovery team, the spacecraft could finally be located using the Deep Space Network Arecibo antenna. Operations to recover the telemetry and check the general status of the spacecraft started. SOHO was back in normal mode again on 25 September 1998. All instruments could be successfully recovered suffering no damage, despite the enormous gradient of temperatures between the sunny and the dark sides of the satellite. Only two of the three gyroscopes were lost during these operations; the third failed over in December 1998. It was then necessary to upload gyroless software that uses reaction wheels to measure the spacecraft roll. SOHO has become the first 3-axis stabilized spacecraft to be operated without a gyroscope.

B Exceptions to the use of the PPN algorithm

The PPN (polar pixel normalization, see Section 2.3.2) algorithm is a hand-made method to detrend LOI data which is based in the hypothesis that polar pixels (1, 2, 3 and 4 in figure 2.3) hardly detect any solar activity because they point to the polar regions of the Sun, far away from the activity belt. This assumption is valid during most of the period covered by LOI 1.0 data. In such cases, the signal detected by the polar pixels is therefore almost free from variations induced by activity and only reproduces the degradation. If we assume that all pixels degrade in the same manner, dividing one pixel signal by the sum of the polar pixels results in a detrended radiance. Therefore, this algorithm considers the radiance of a given pixel divided by the sum of the radiances of the four polar pixels. This method produces the best results for long periods of data. However, we must be very careful when choosing the time interval, because solar activity increases considerably at the end of 1997, when even pixels 1, 2, 3 and 4 detect the passage of active regions.

The following figures show exceptions to the usage of this algorithm. In these cases this method can not be used since even polar pixels detect the passage of active regions. This activity jeopardizes the result of the normalization. Afortunatly, the period covered by LOI 1.0 data only contains the few exceptions shown in figures B.1, B.2 and B.3.

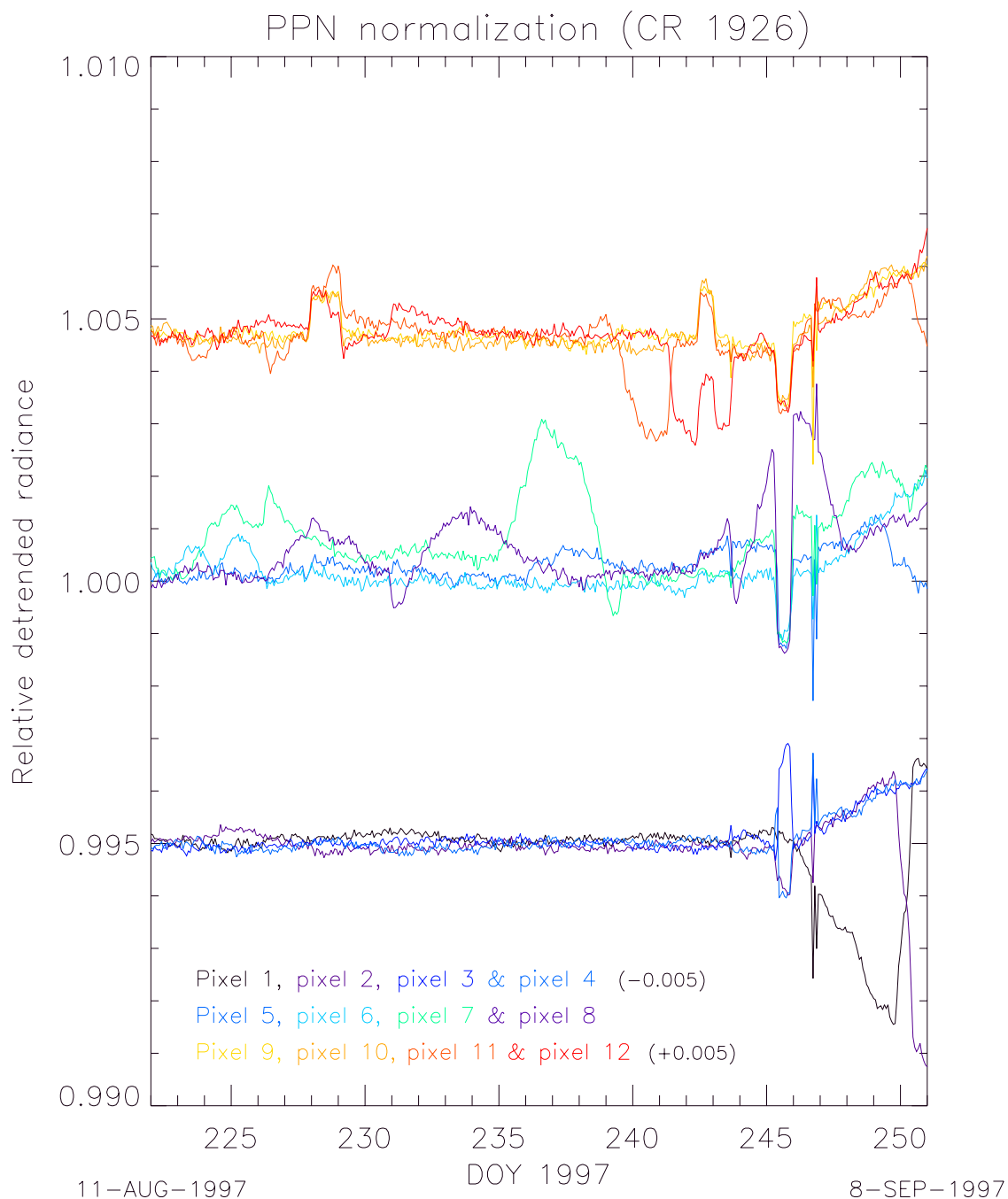


Figure B.1: LOI 1.0 data (pixels 5 to 12) detrended by means of the polar pixel normalization algorithm, for Carrington rotation 1926. For clarity, radiances have been separated by 0.005 units. The radiance of pixels 1 to 4 is also shown; even these pixels detect the passage of solar activity.

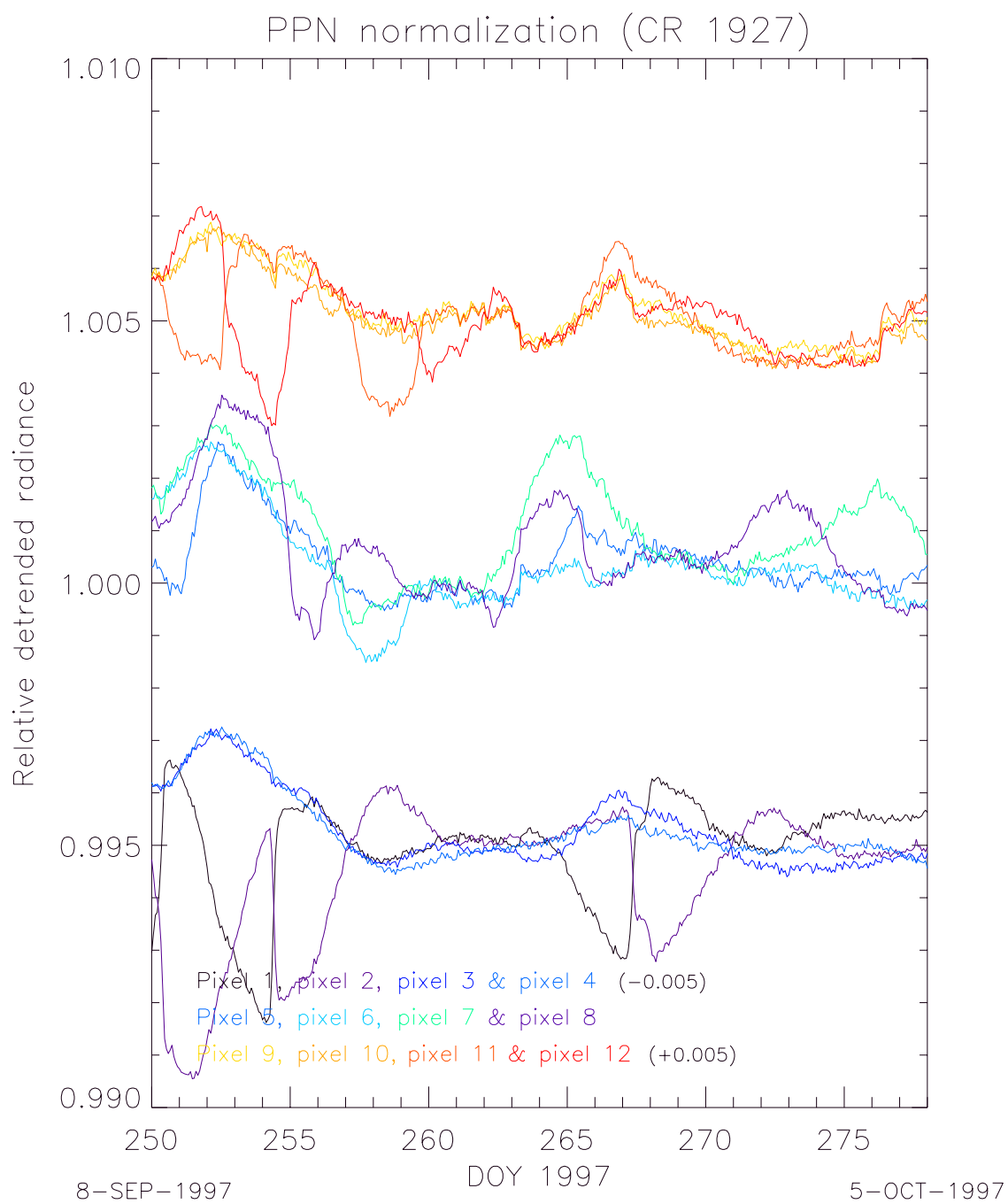


Figure B.2: Same as figure B.1 for Carrington rotation 1927.

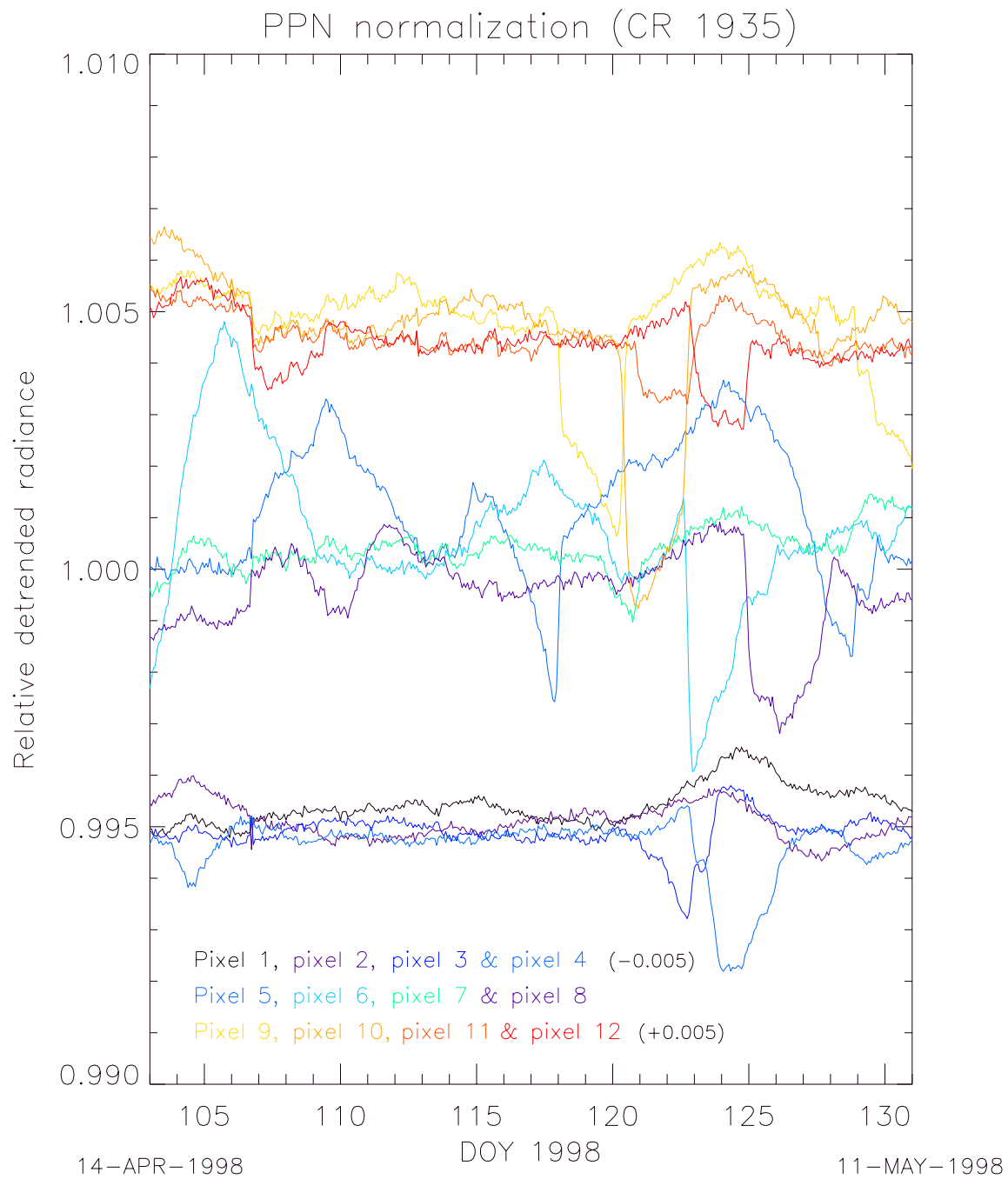


Figure B.3: Same as figure B.1 for Carrington rotation 1935.

C Evolution of the facular contrast with the solar cycle

The following figures show the evolution along more than half a solar cycle of the AR faculae and network contrast dependence on both μ and the measured magnetic signal, B/μ , corrected for foreshortening effects. Figure C.1 illustrates some sample full-disk magnetograms provided by MDI (left panels). The results of applying the contrast masks are displayed on the right panels. Only features that lie above the given thresholds (see Chapters 4 and 5) are indicated as black pixels. These masks identify small-scale bright magnetic features over the solar surface and give their contrast. It can be clearly seen the increase of magnetic activity as the solar cycle approaches its maximum. Figures C.2 to C.7 represent the contrast as a function of μ , the contrast CLV, sorting the magnetic signal into eight intervals from network values to strong faculae, for the period 1996-2001. Figures C.8 to C.13 show the dependence of the contrast on the absolute value of the magnetogram signal (corrected for foreshortening effects) for the same time interval. The solar disk has been divided into eight bins, from center to limb.

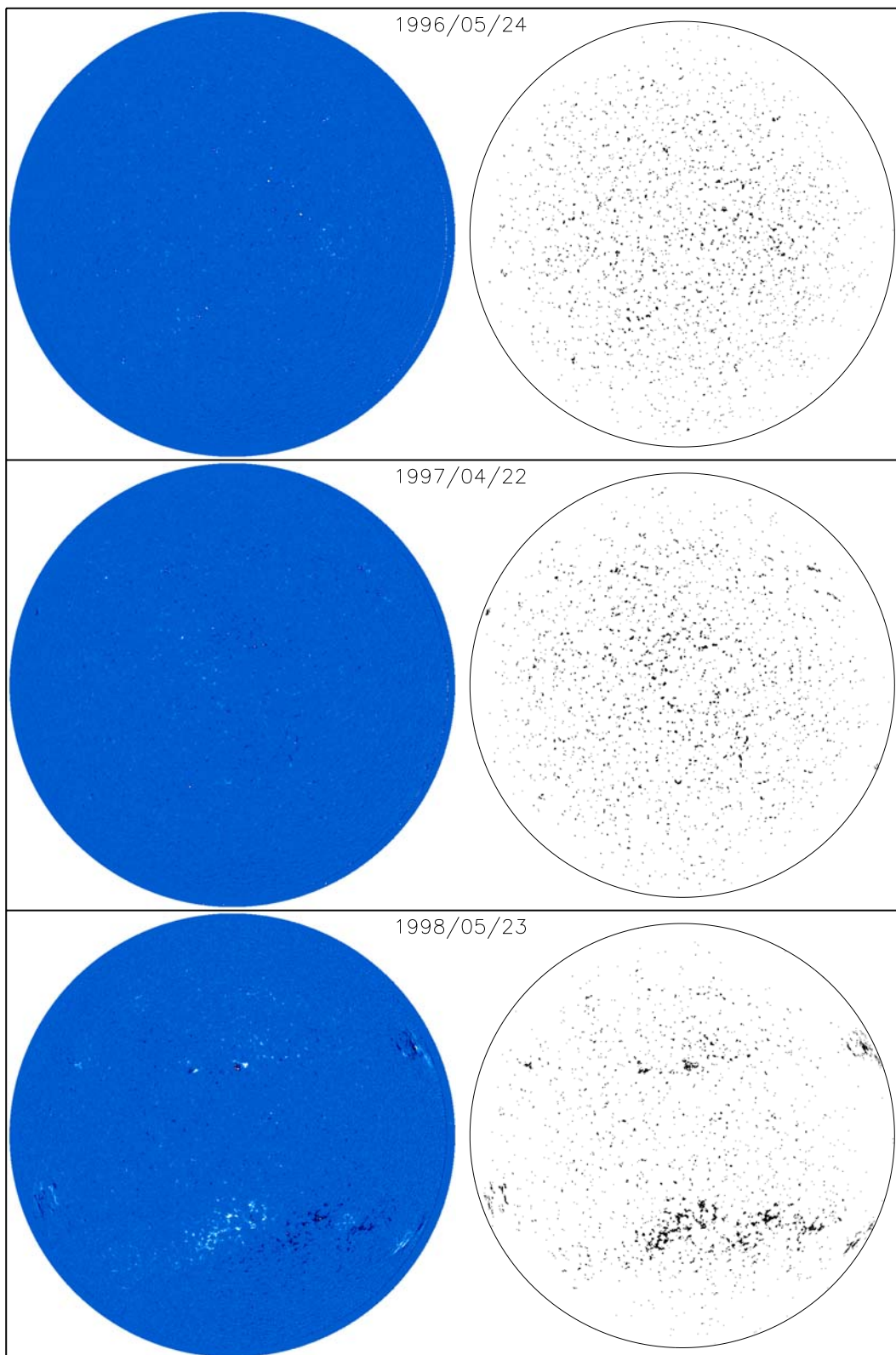


Figure C.1: Example of MDI magnetograms (left panels) and the resulting contrast masks (right panels) at different phases of the rising phase of cycle 23, from 1996 to 2001.

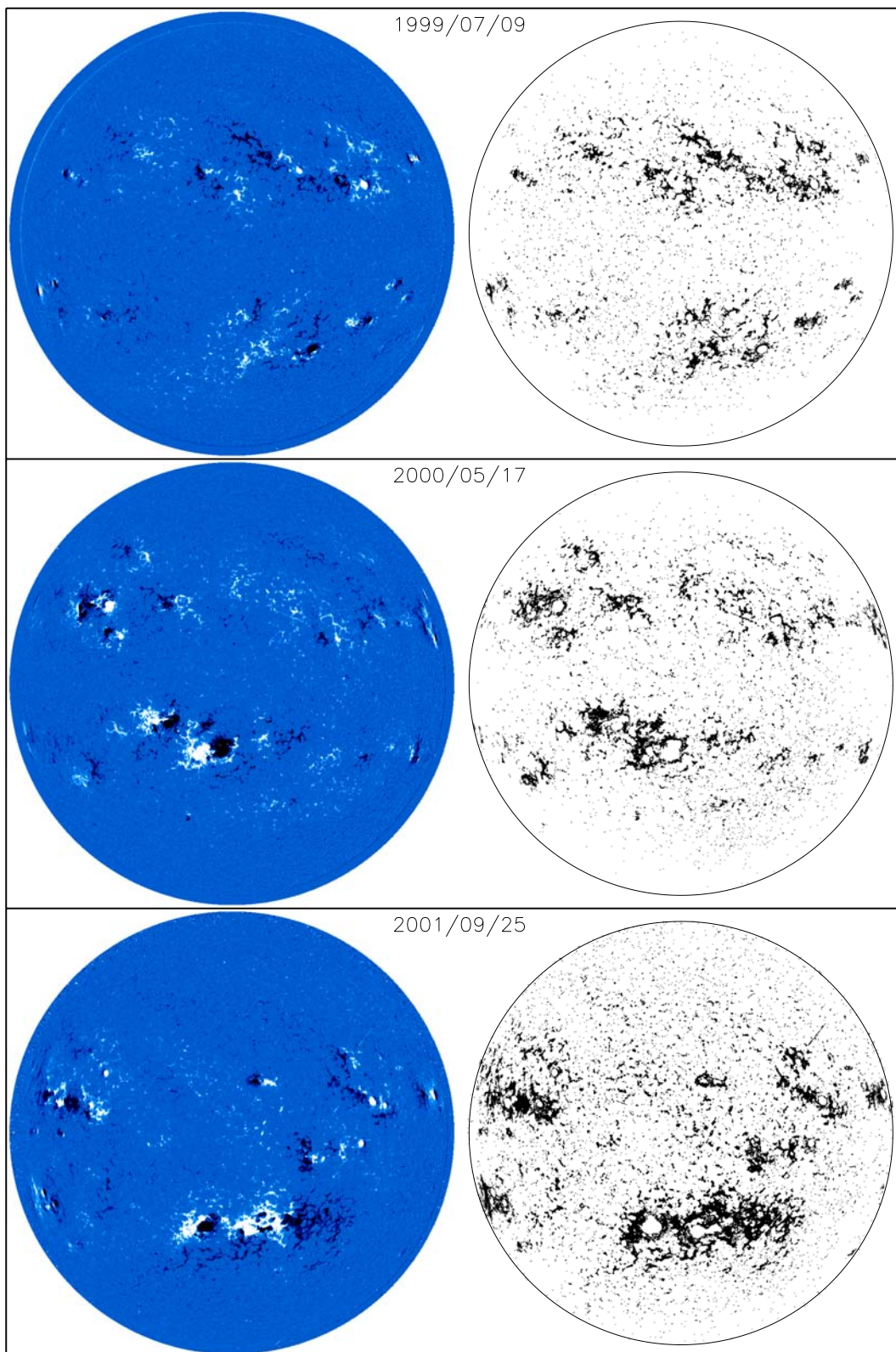


Figure C.1: Continued.

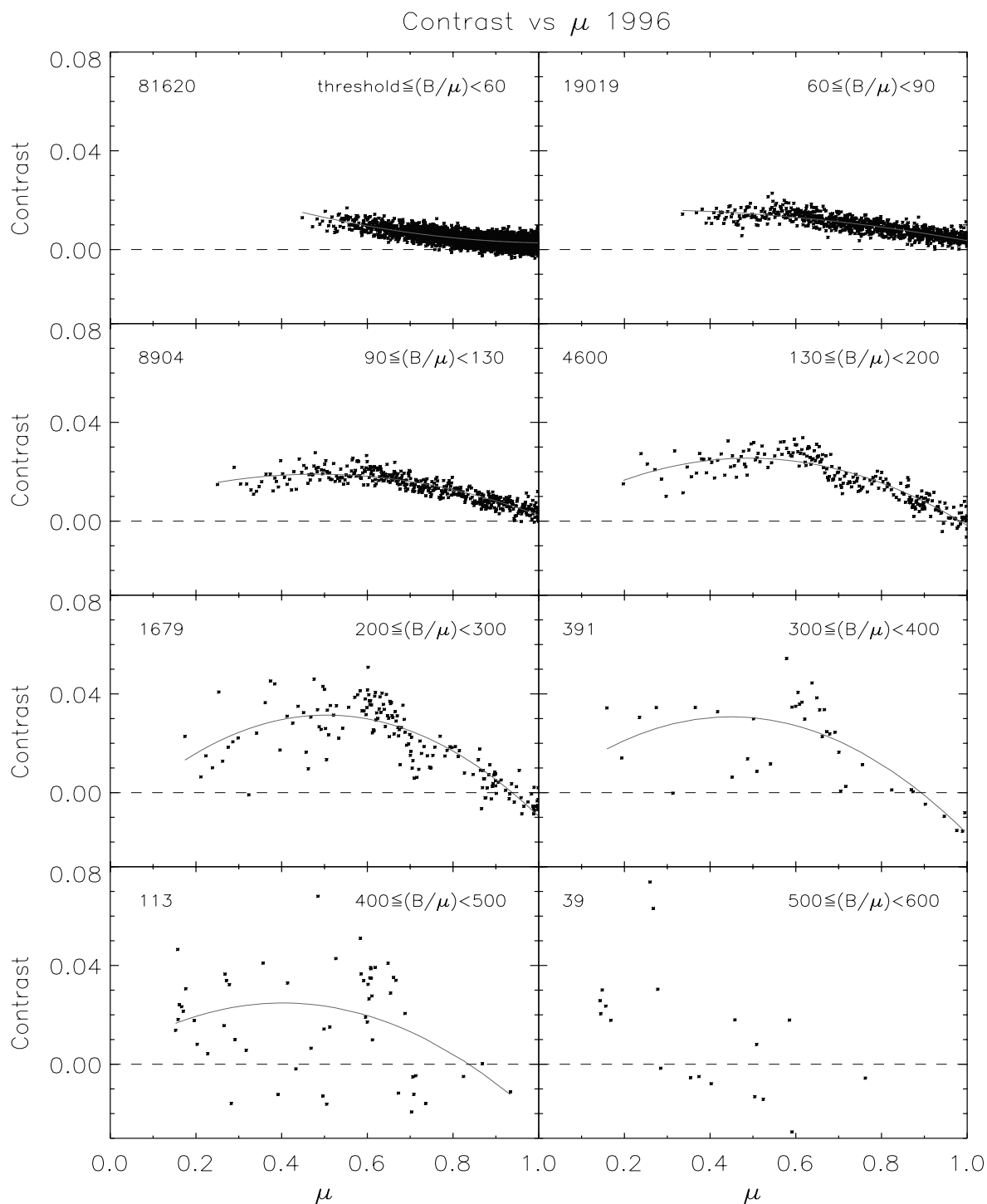


Figure C.2: Facular and network contrast at solar minimum (1996) as a function of μ for eight magnetic field intervals, from network values (top left panel) to strong faculae (lower right). A dashed line at $C_{\text{fac}} = 0$ has been plotted. Solid curves represent a second degree polynomial least-squares fit to the points. $\mu = 1$ is the disk center; $\mu = 0$ is the limb. Numbers in the upper left corner of each interval indicate the amount of pixels in the given B/μ interval.

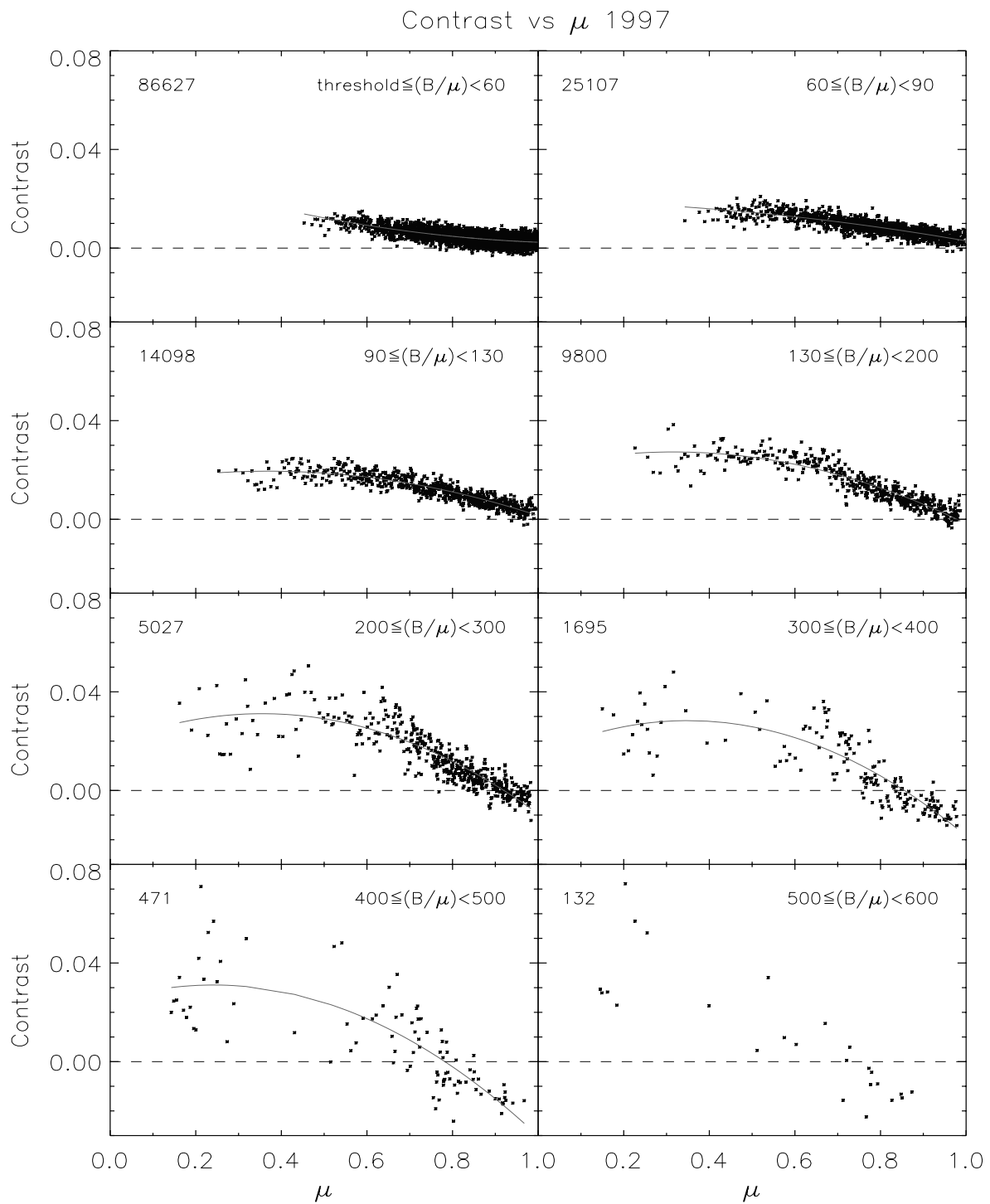


Figure C.3: The same as figure C.2 for 1997.

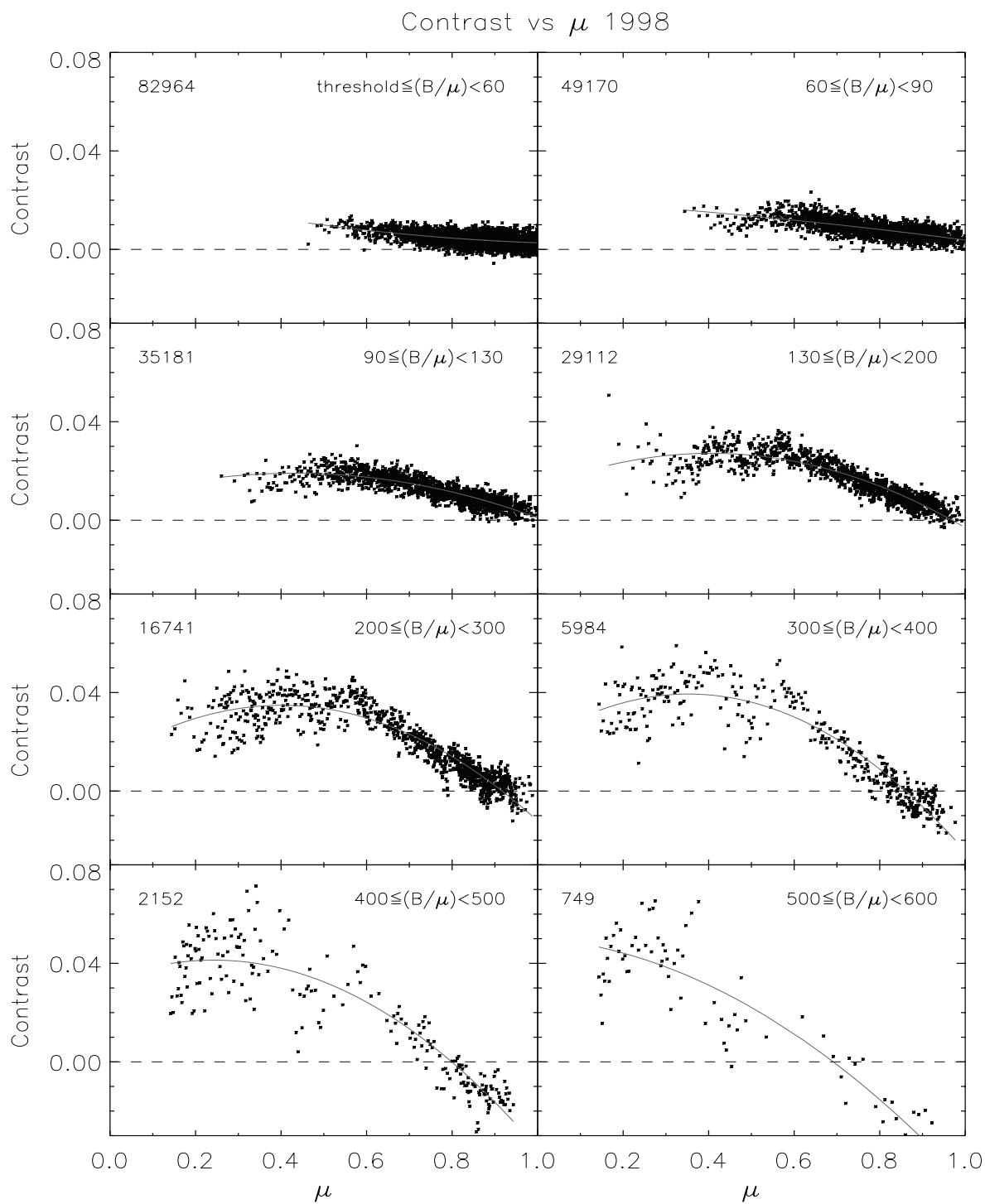


Figure C.4: The same as figure C.2 for 1998.

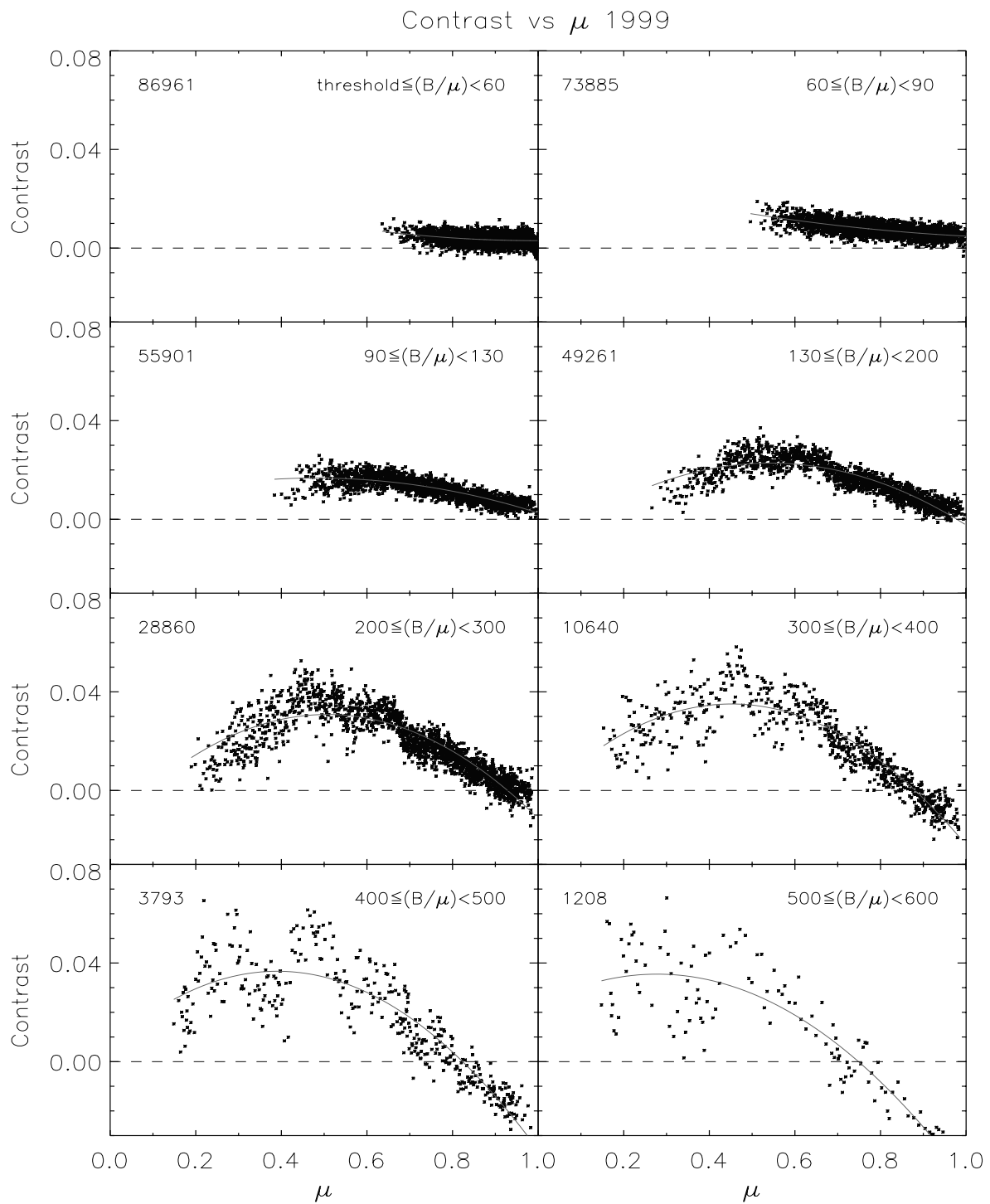


Figure C.5: The same as figure C.2 for 1999.

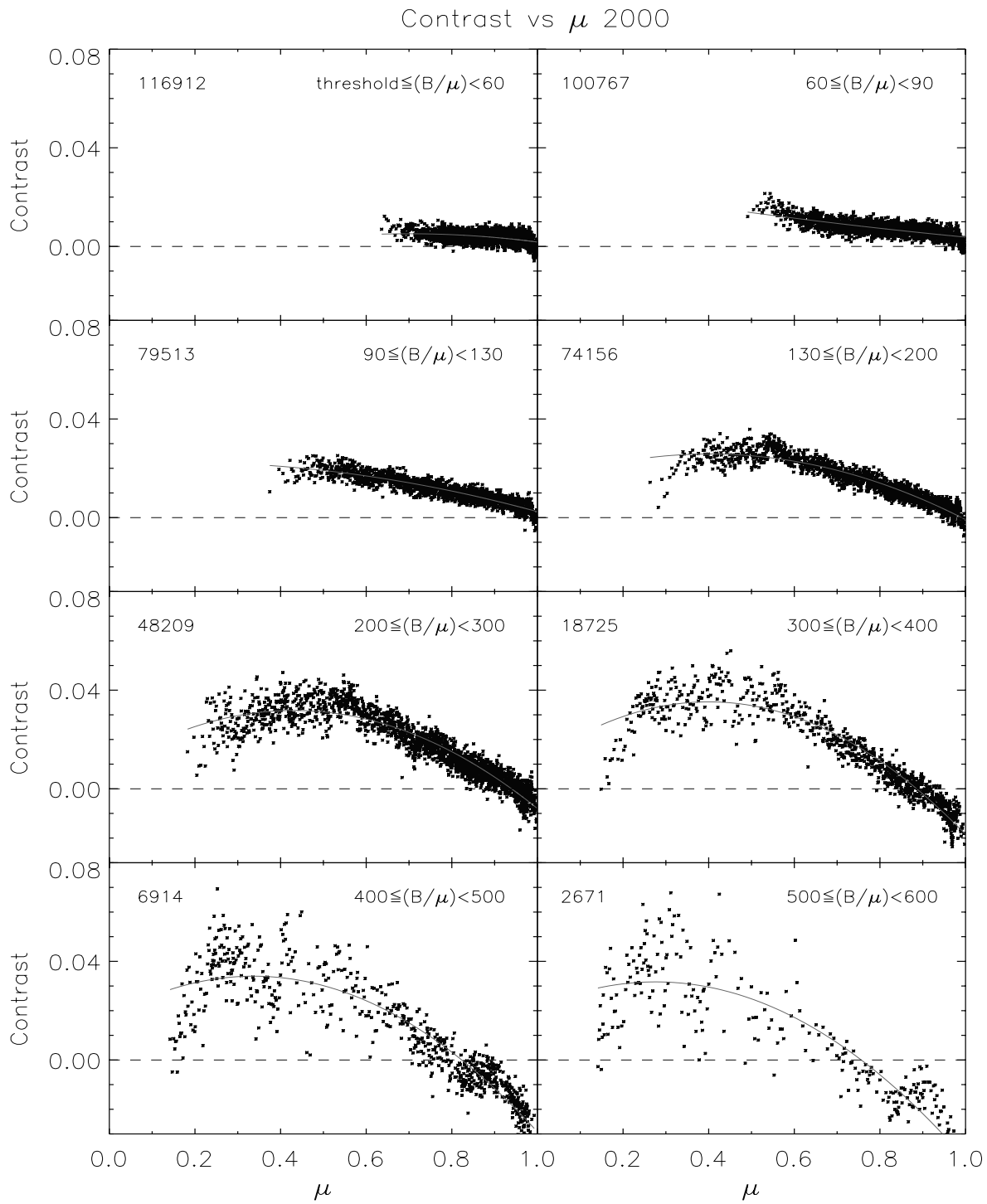


Figure C.6: The same as figure C.2 for 2000.

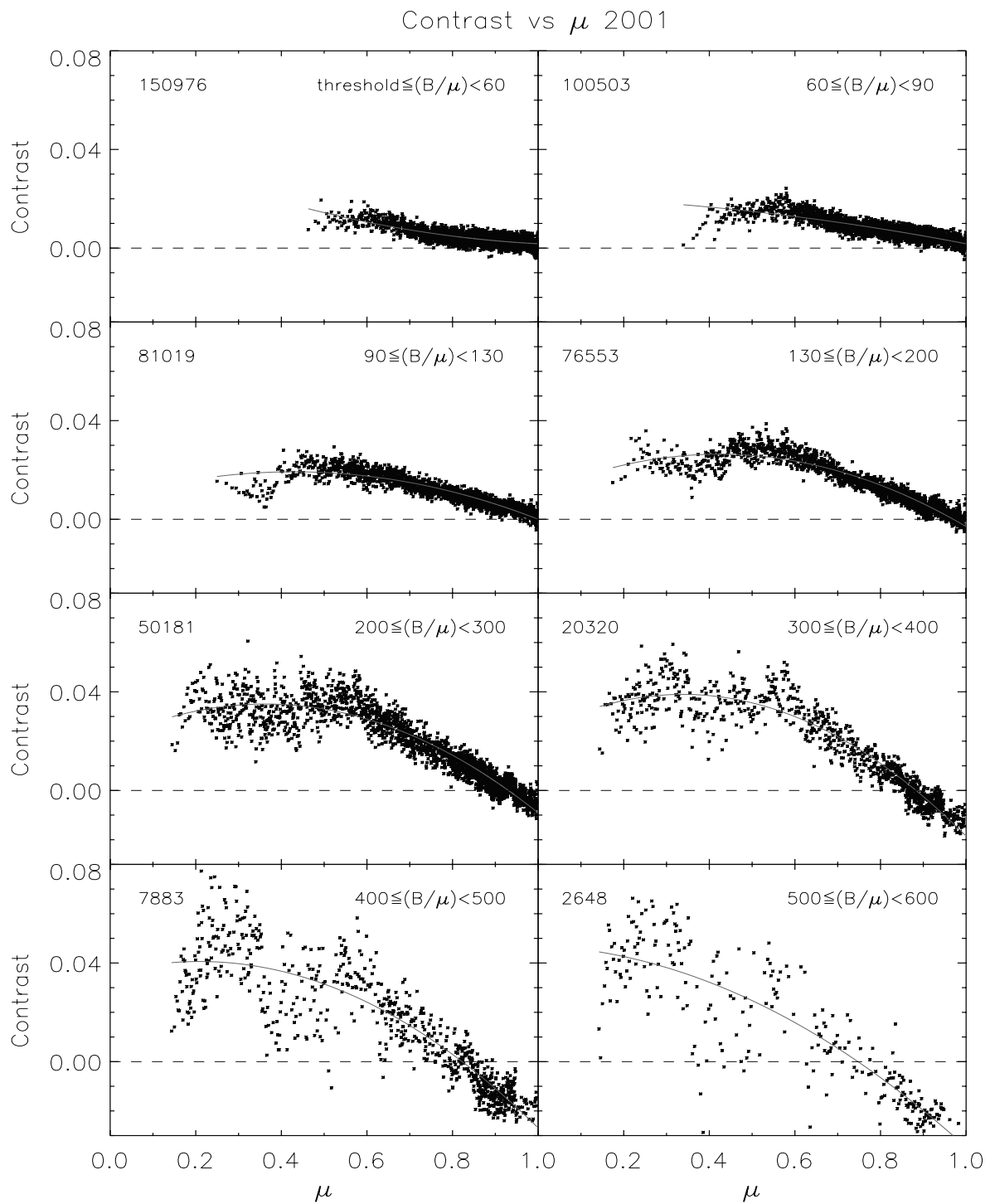


Figure C.7: The same as figure C.2 for 2001.

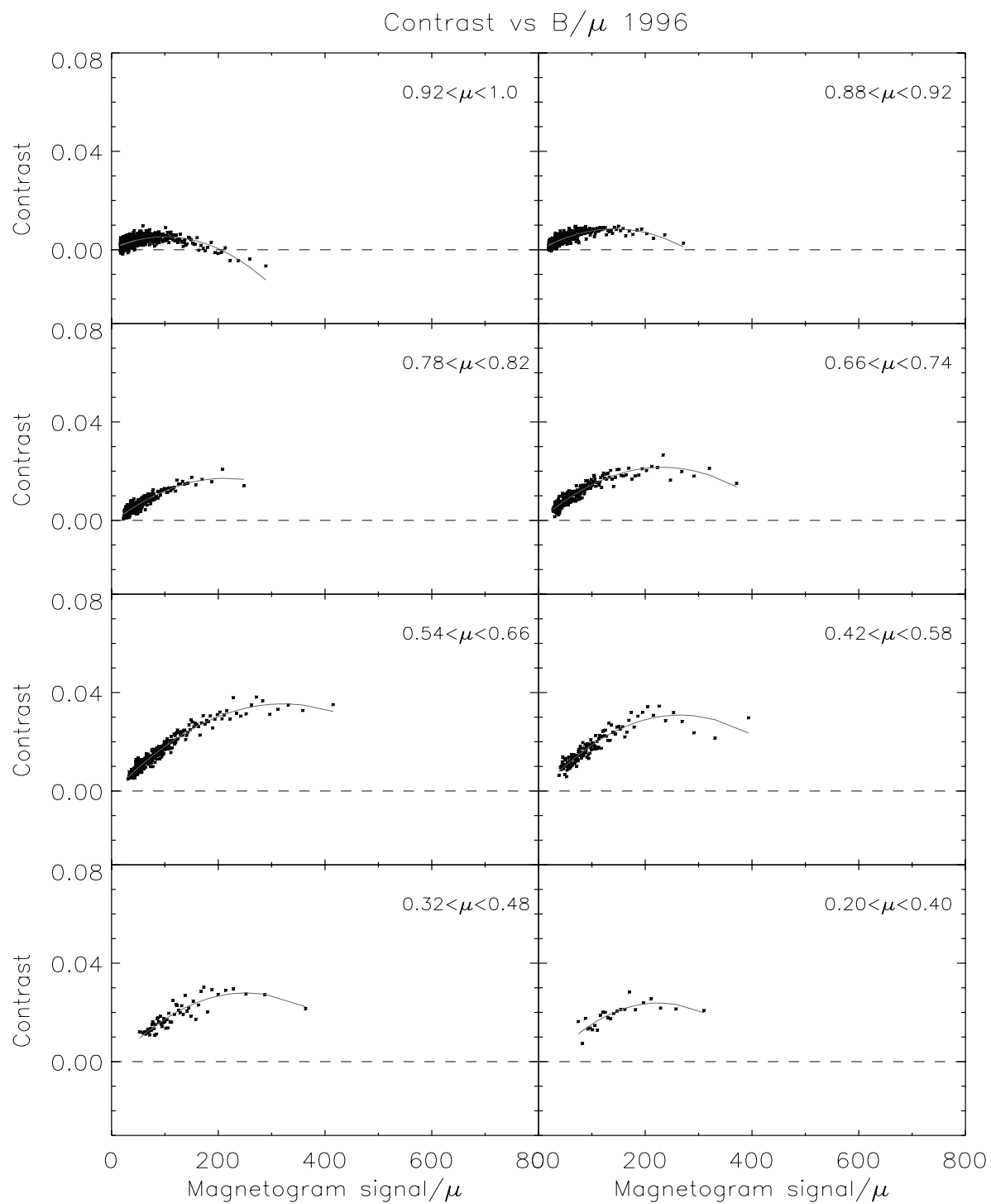


Figure C.8: Dependence of the contrast on the absolute value of the magnetogram signal (corrected for foreshortening effects) for 1996. The solar disk has been divided into eight bins, from center to limb. Note that some μ -bins overlap. Solid curves represent a quadratic fit to the points.

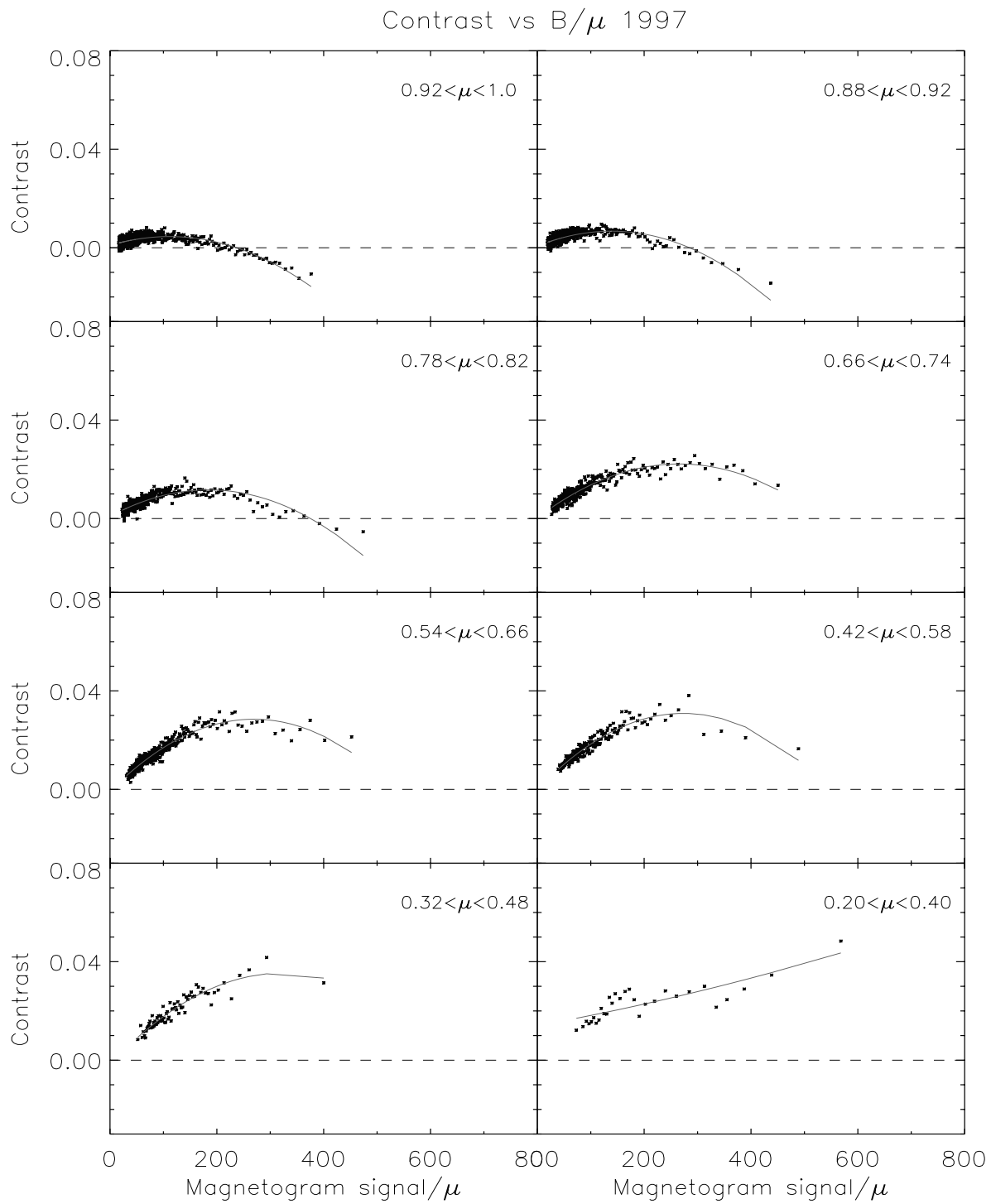


Figure C.9: The same as figure C.8 for 1997.

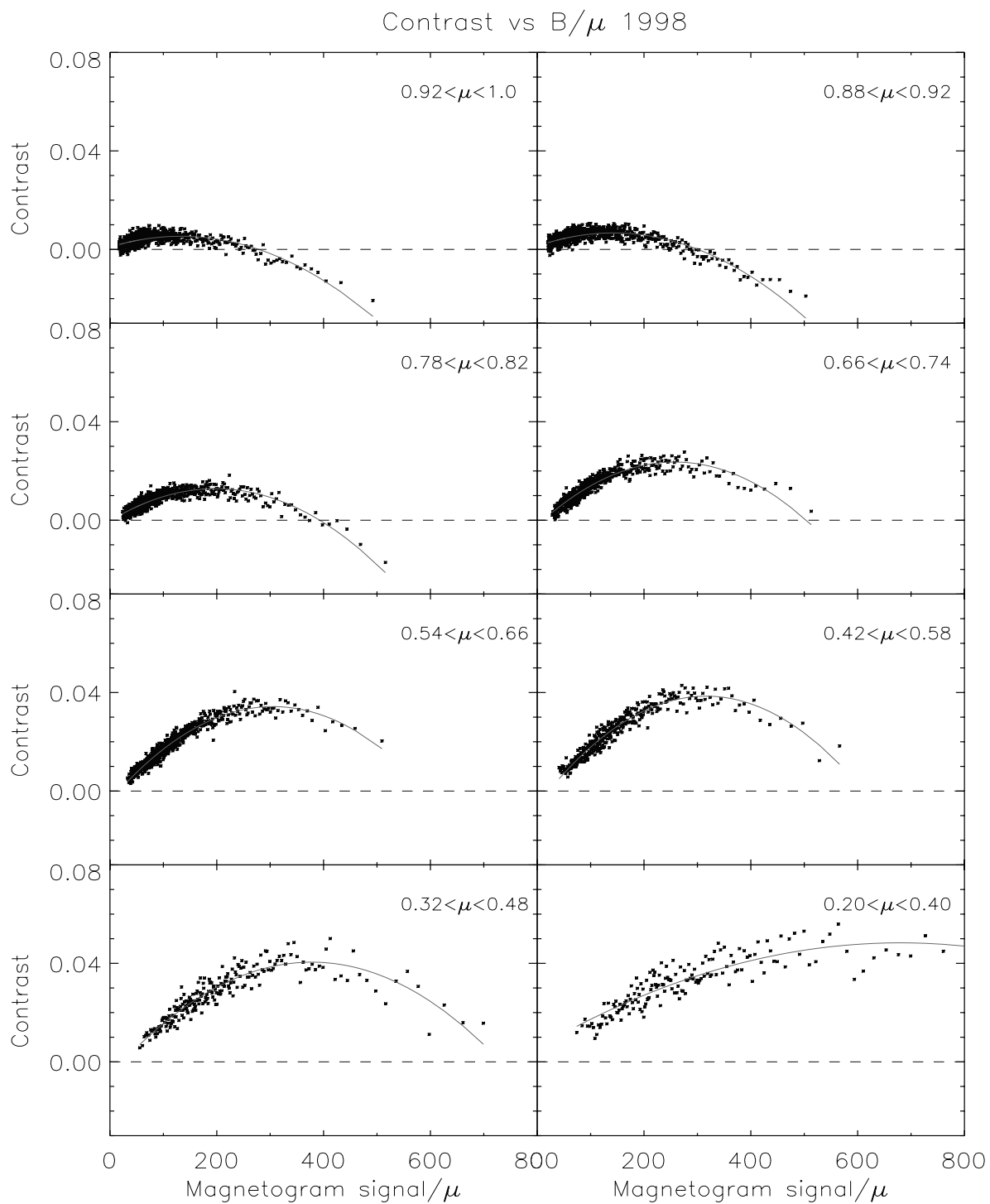


Figure C.10: The same as figure C.8 for 1998.

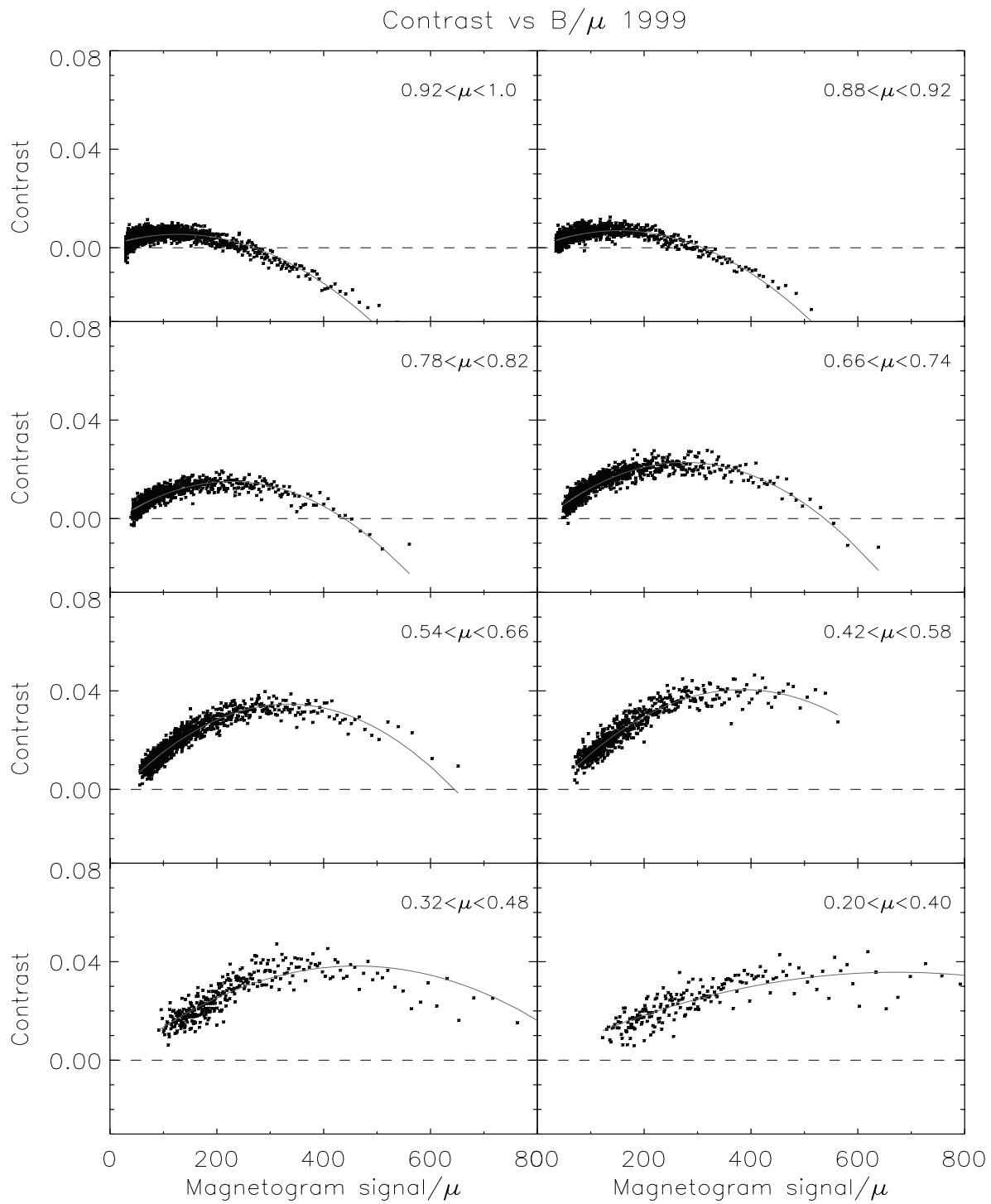


Figure C.11: The same as figure C.8 for 1999.

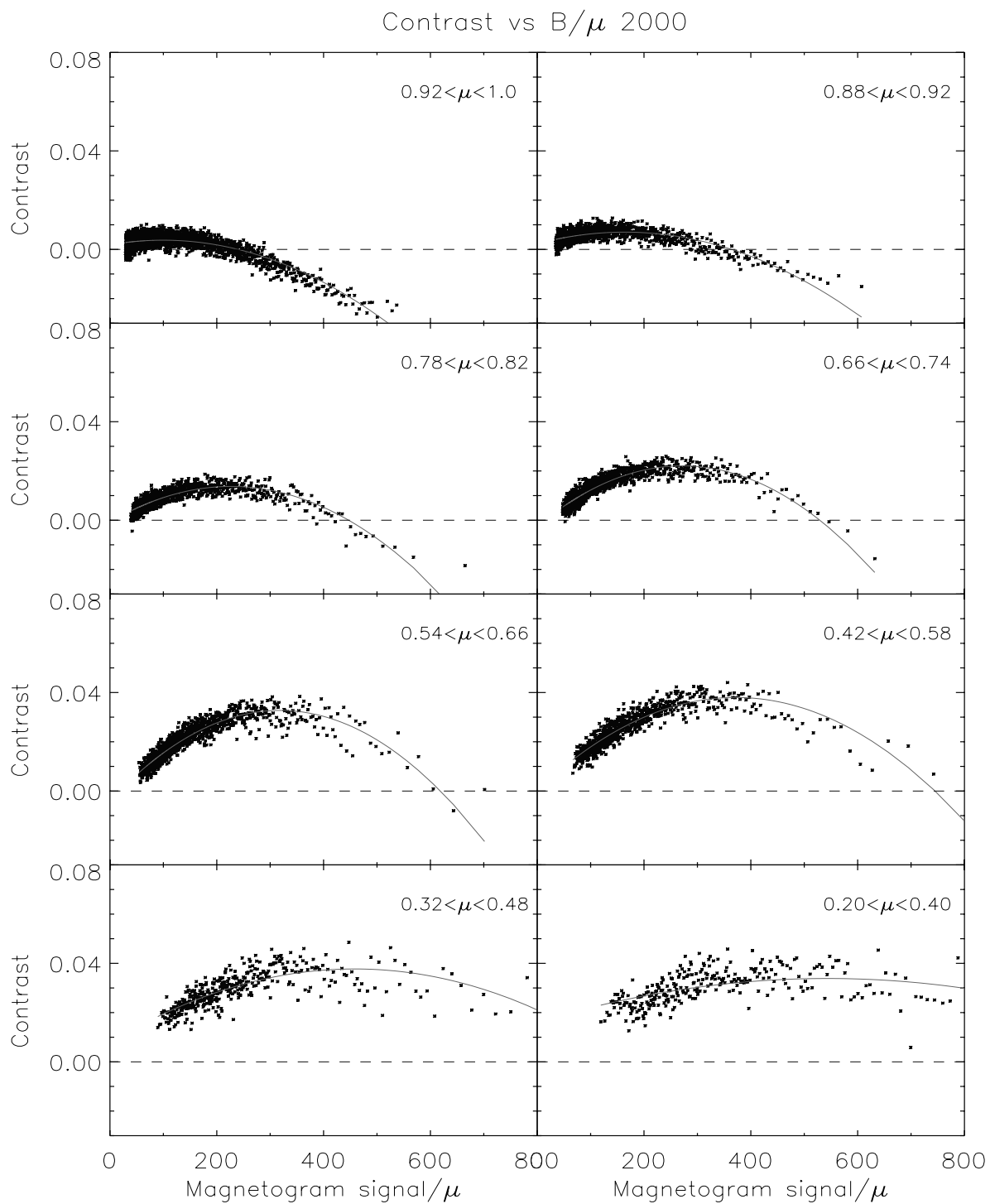


Figure C.12: The same as figure C.8 for 2000.

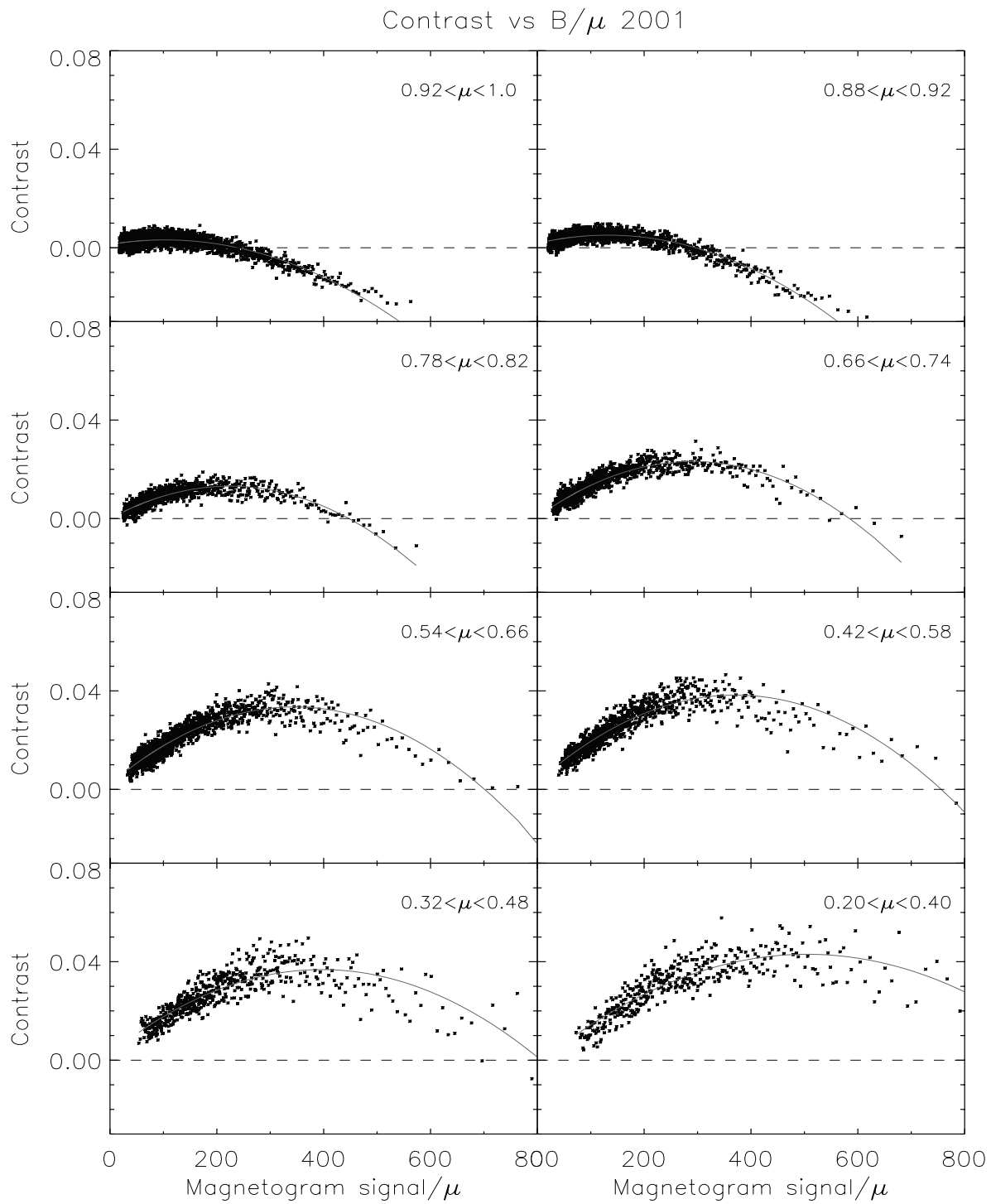


Figure C.13: The same as figure C.8 for 2001.

D Contrast evolution of the AR and QS components with the solar cycle

The following figures show the evolution of the contrast of the active region (AR) and quiet Sun (QS) components in which the solar surface has been decomposed (see Chapter 5), for more than half a solar cycle. Figures D.1 to D.6 represent the contrast as a function of μ , the contrast CLV, sorting the magnetic signal into eight intervals. We have divided the studied period in three subperiods, named “Minimum”, “Mid” and “Maximum” (see Section 5.3.3). Active region and quiet Sun structure classes are denoted as “AR” and “QS”, respectively. Figures D.7 to D.12 show the dependence of the contrast on the absolute value of the magnetogram signal (corrected for foreshortening effects) for the same subperiods and components.

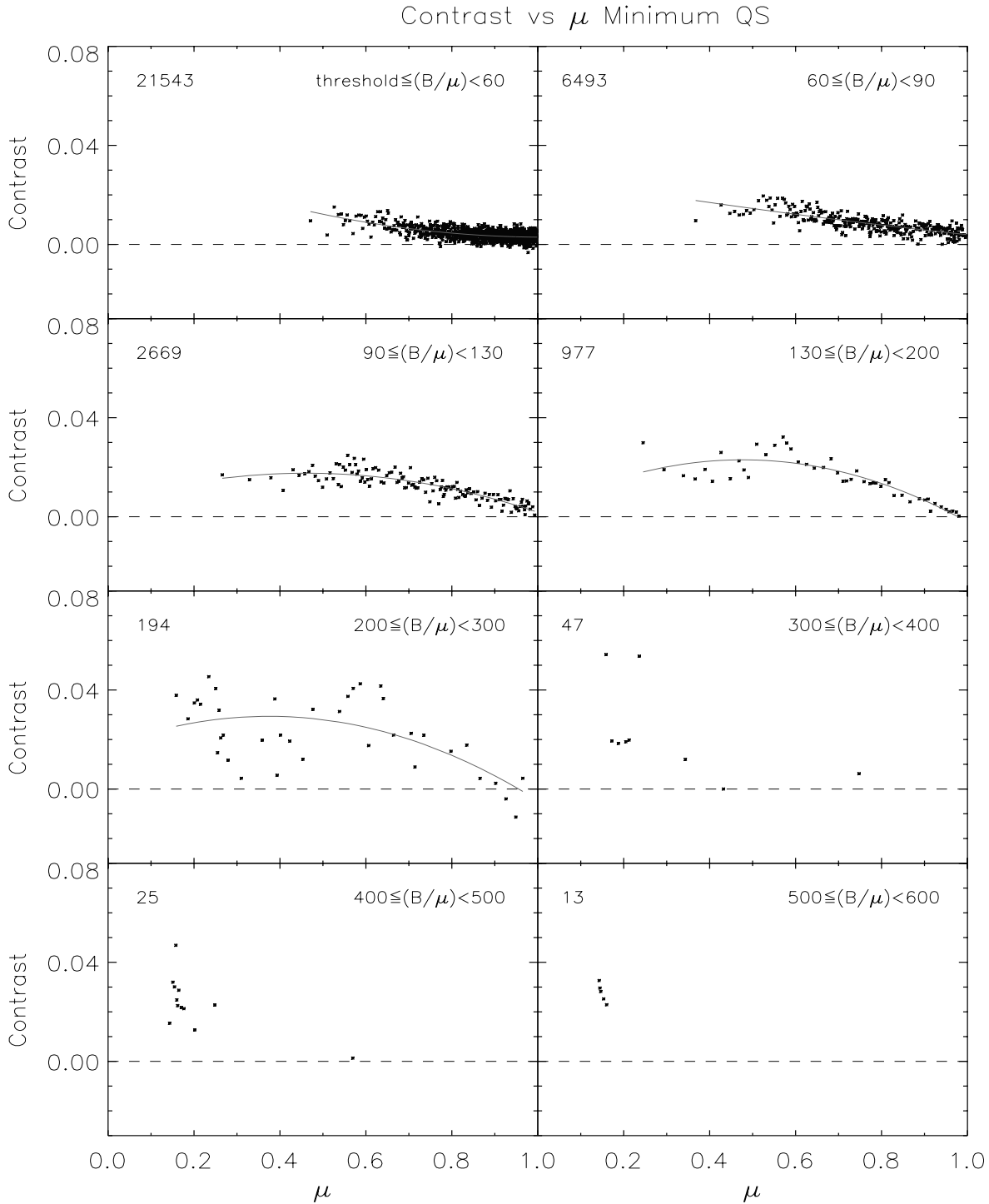


Figure D.1: Contrast of the quiet Sun component around the solar minimum, as a function of μ for eight magnetic field intervals. A dashed line at $C_{\text{fac}} = 0$ has been plotted. Solid curves represent, when possible, a second degree polynomial least-squares fit to the points. $\mu = 1$ is the disk center; $\mu = 0$ is the limb. Numbers in the upper left corner of each interval indicate the amount of pixels in the given B/μ interval.

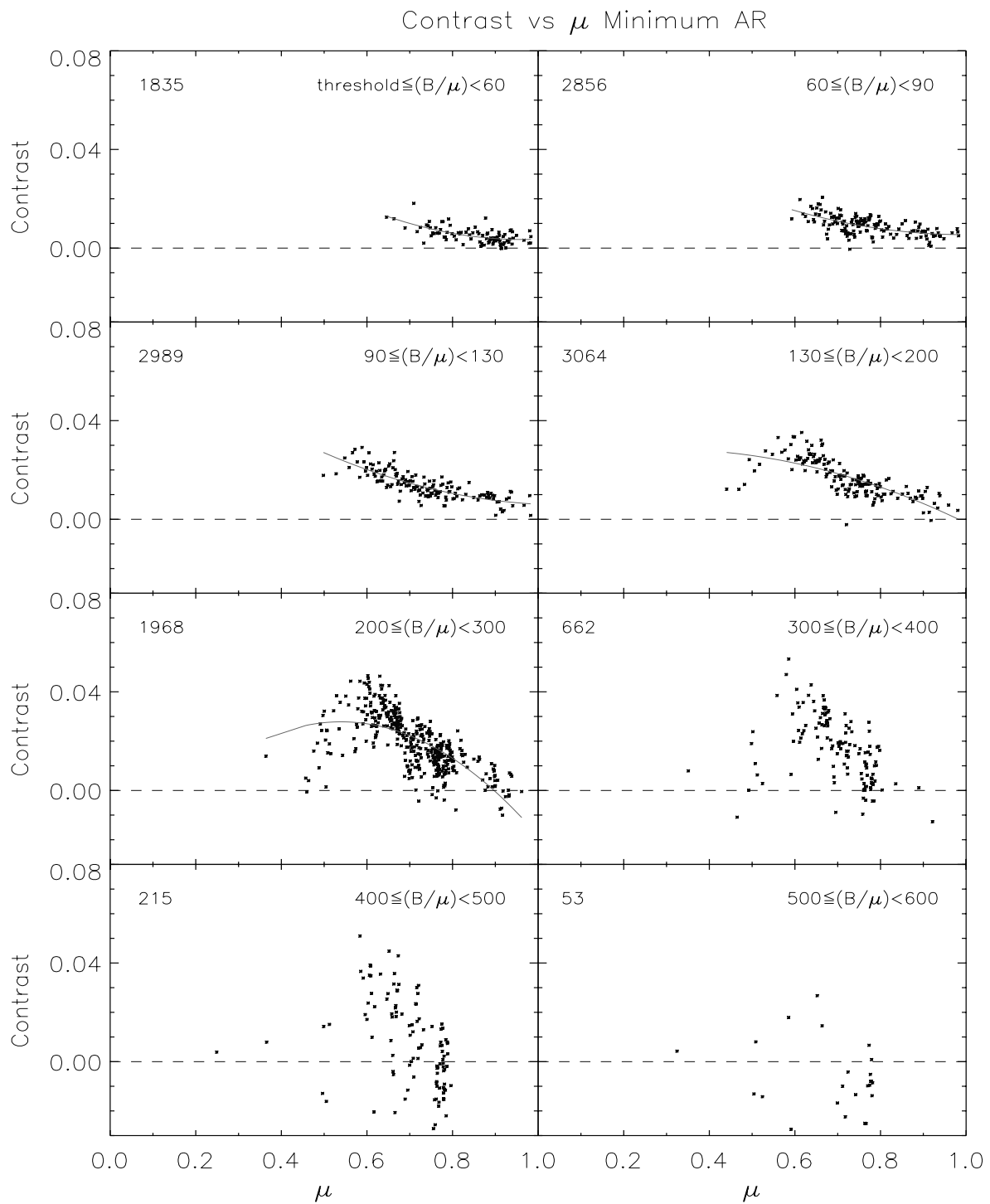


Figure D.2: The same as figure D.1 for the AR component at the minimum.

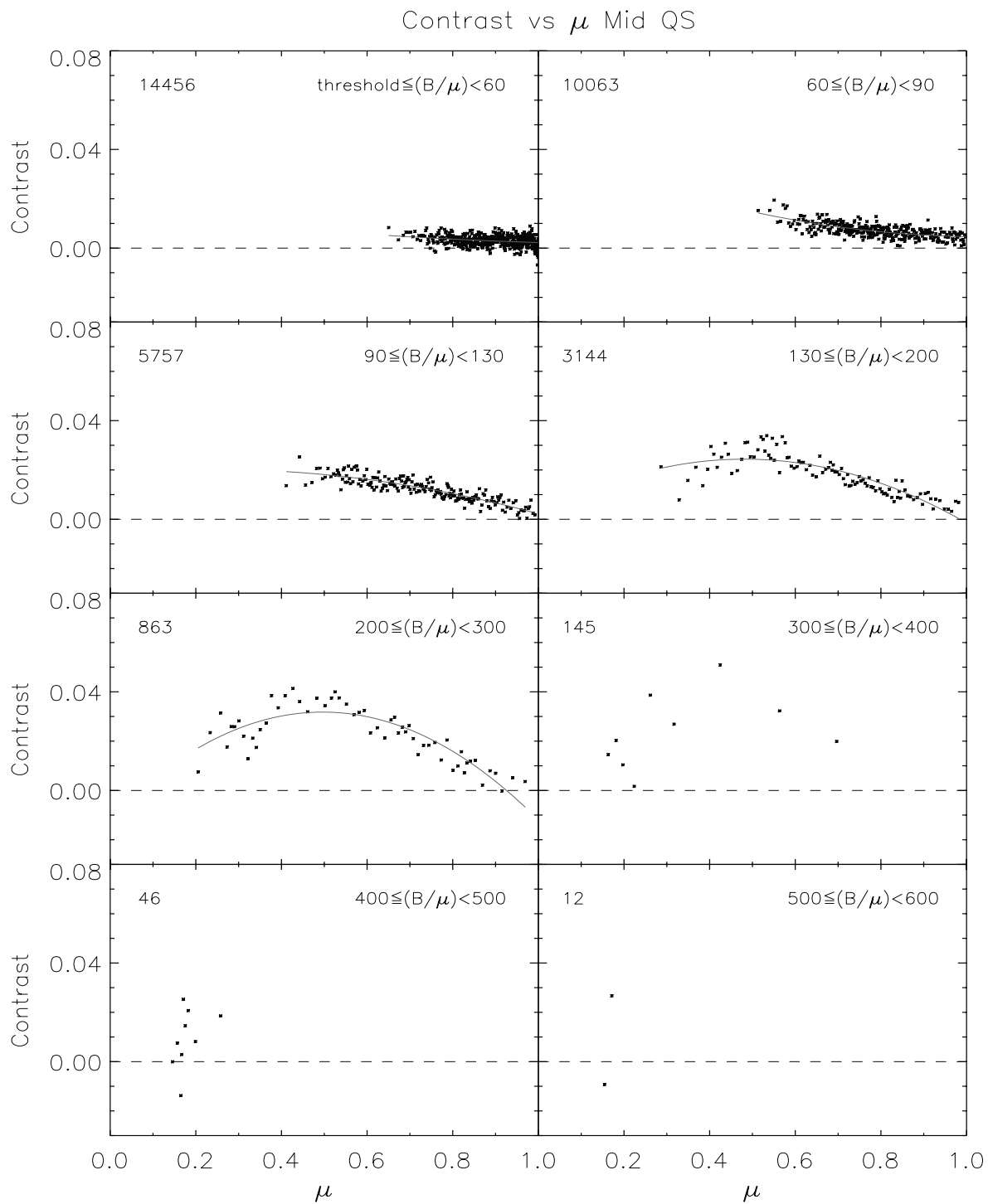


Figure D.3: The same as figure D.1 for the QS component at mid cycle.

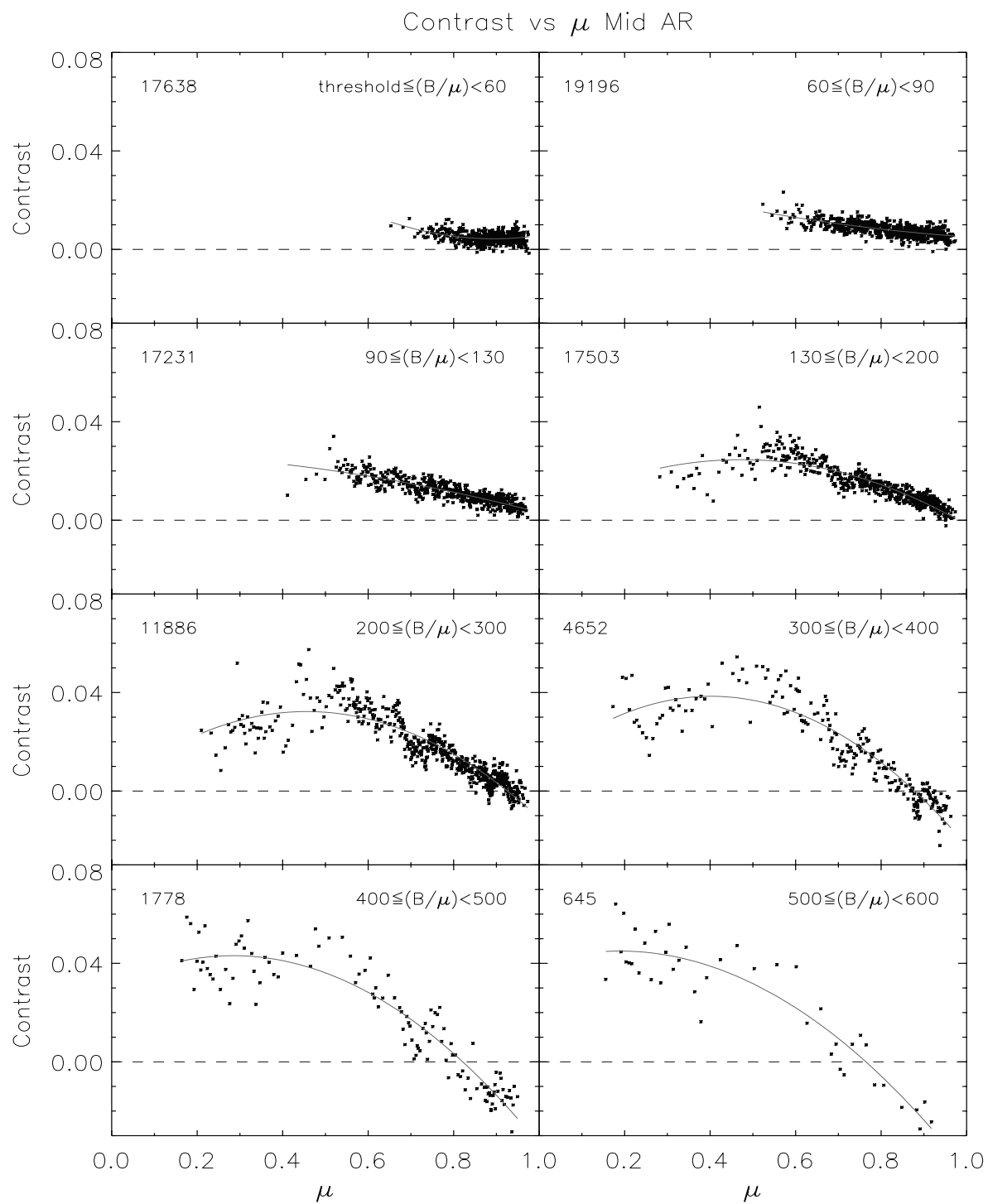


Figure D.4: The same as figure D.1 for the AR component at mid cycle.

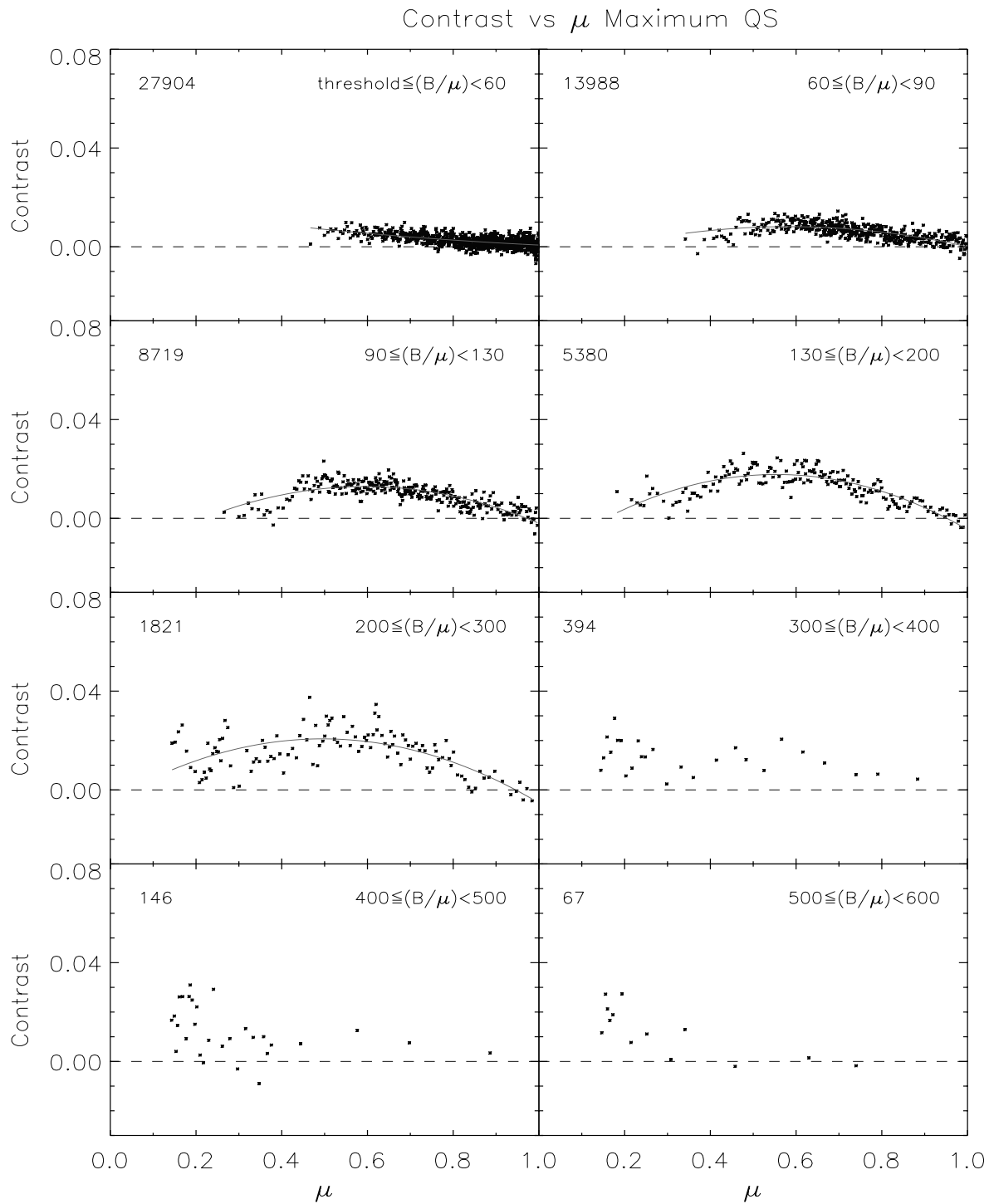


Figure D.5: The same as figure D.1 for the QS component at the maximum.

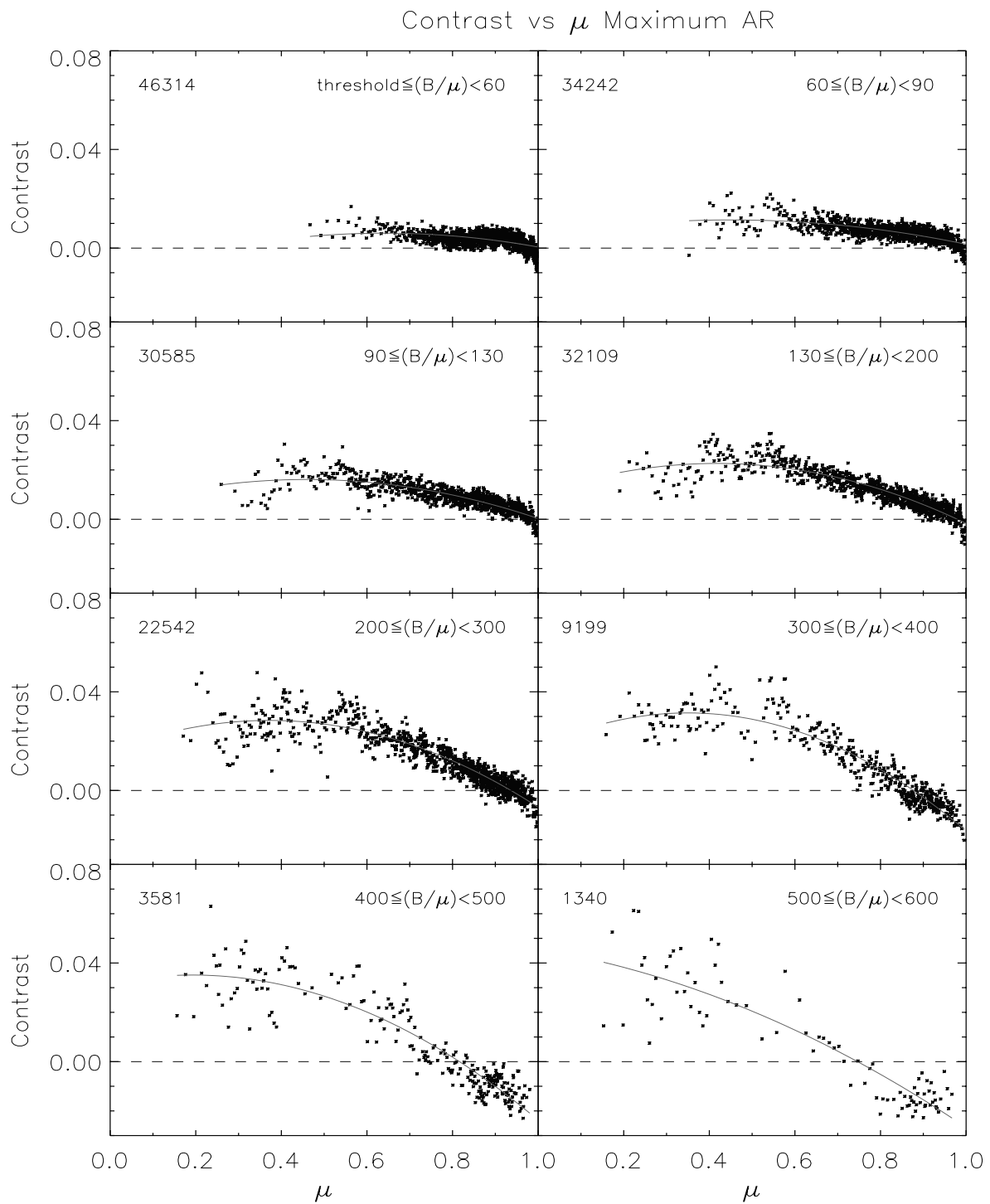


Figure D.6: The same as figure D.1 for the AR component at the maximum.

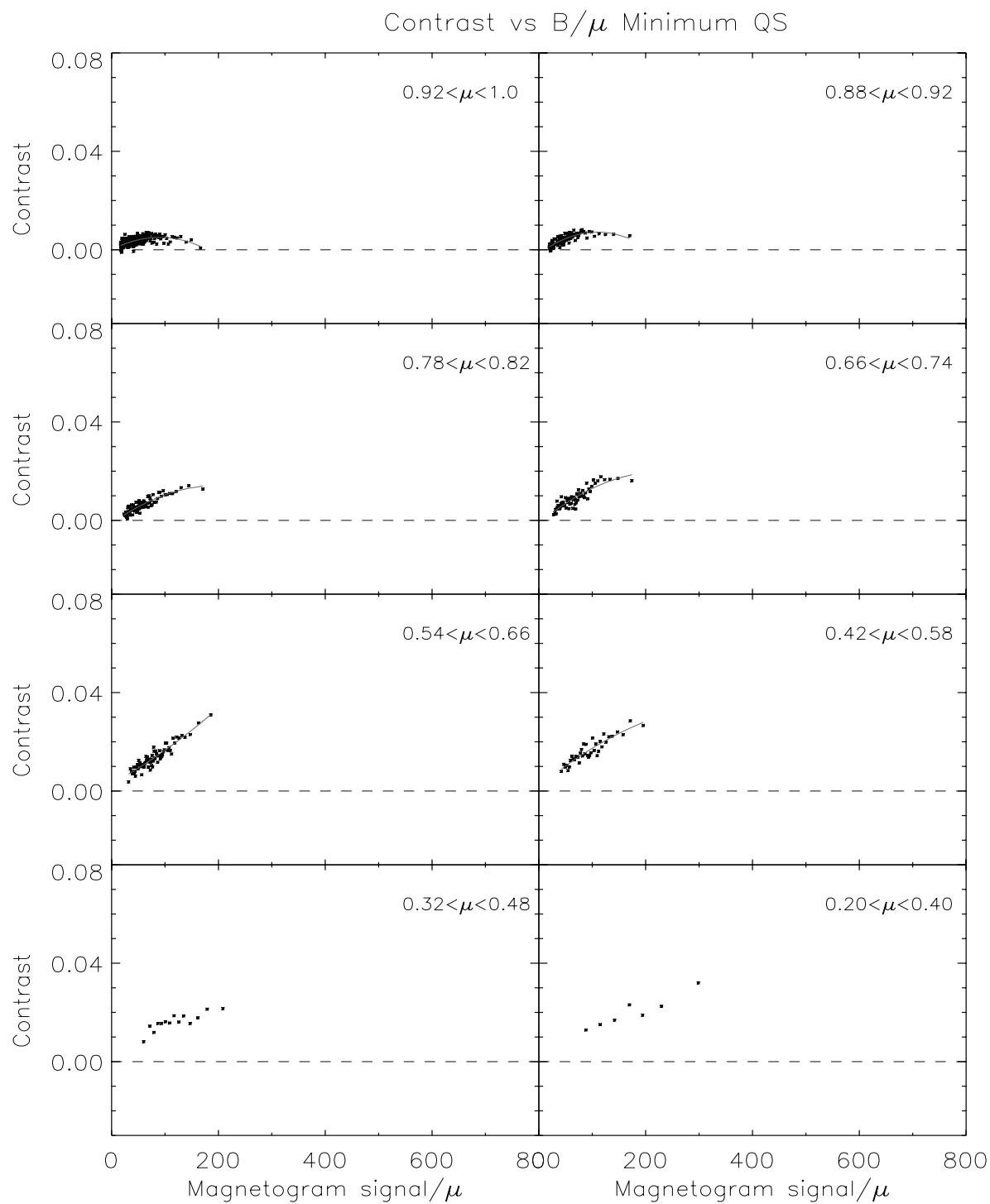


Figure D.7: Dependence of the QS component contrast on the absolute value of the magnetogram signal (corrected for foreshortening effects) around the solar minimum. The solar disk has been divided into eight bins, from center to limb. Note that some μ -bins overlap. Solid curves represent a quadratic fit to the points, when possible.

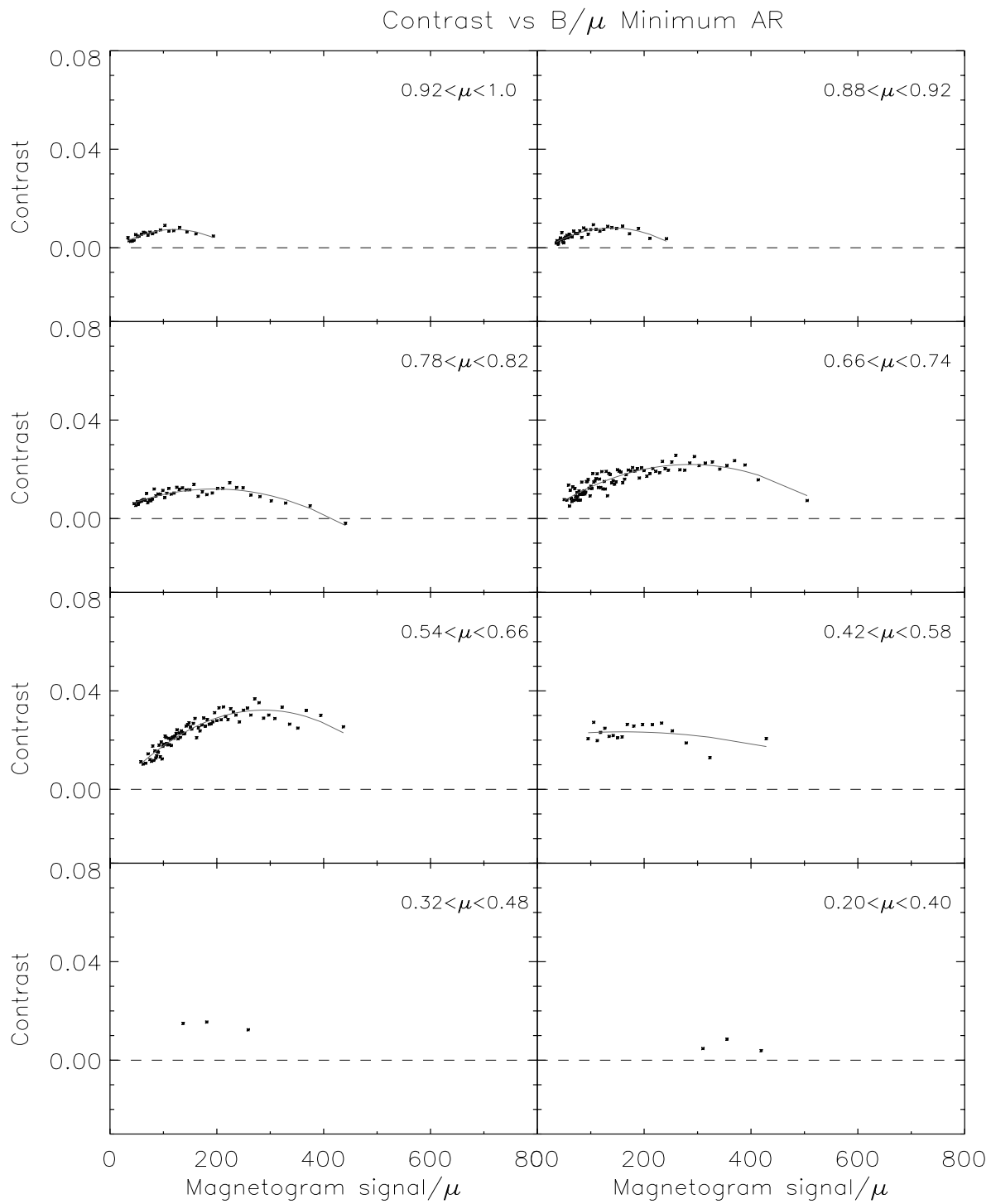


Figure D.8: The same as figure D.7 for the AR component at solar minimum.

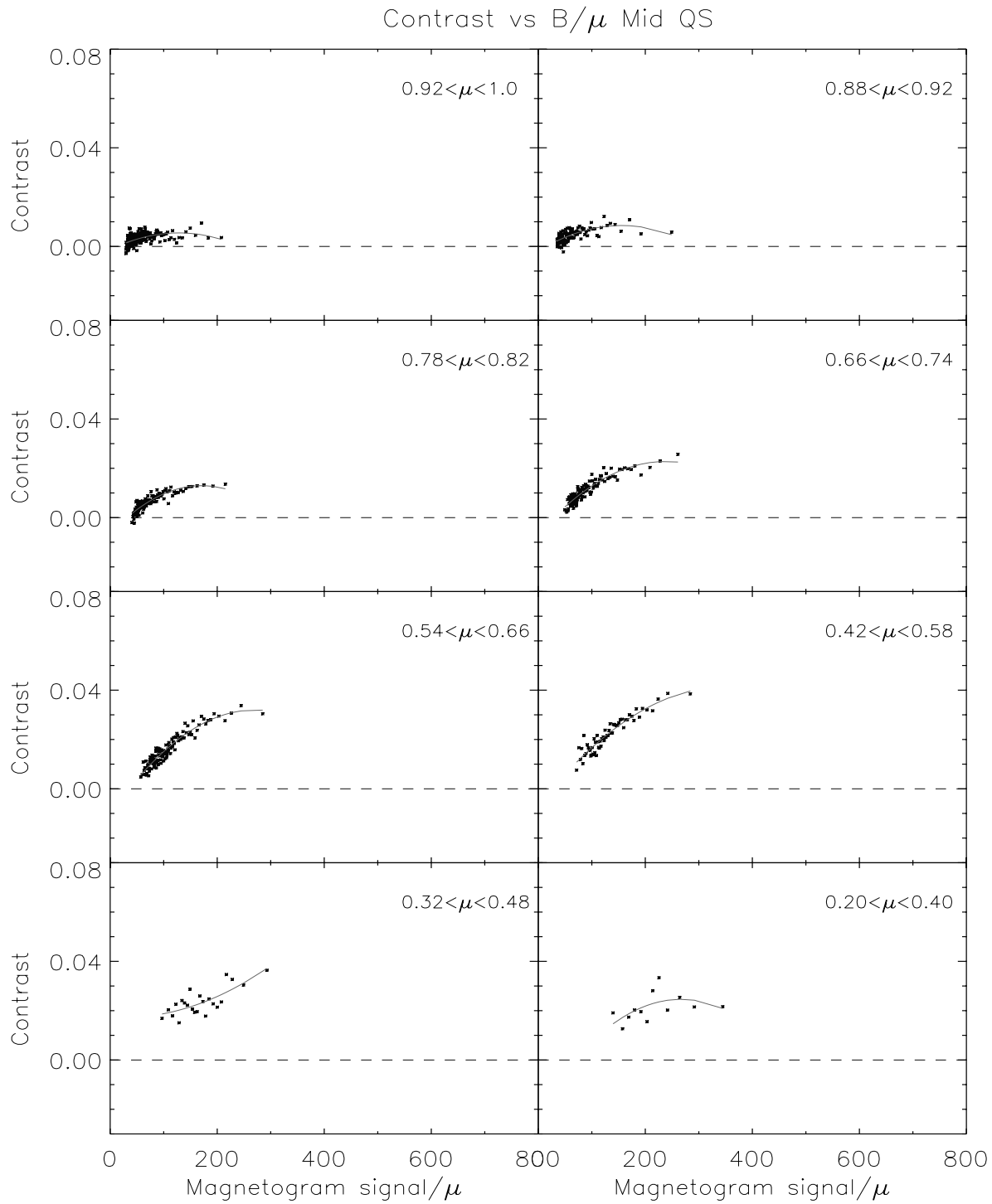


Figure D.9: The same as figure D.7 for the QS component at mid cycle.

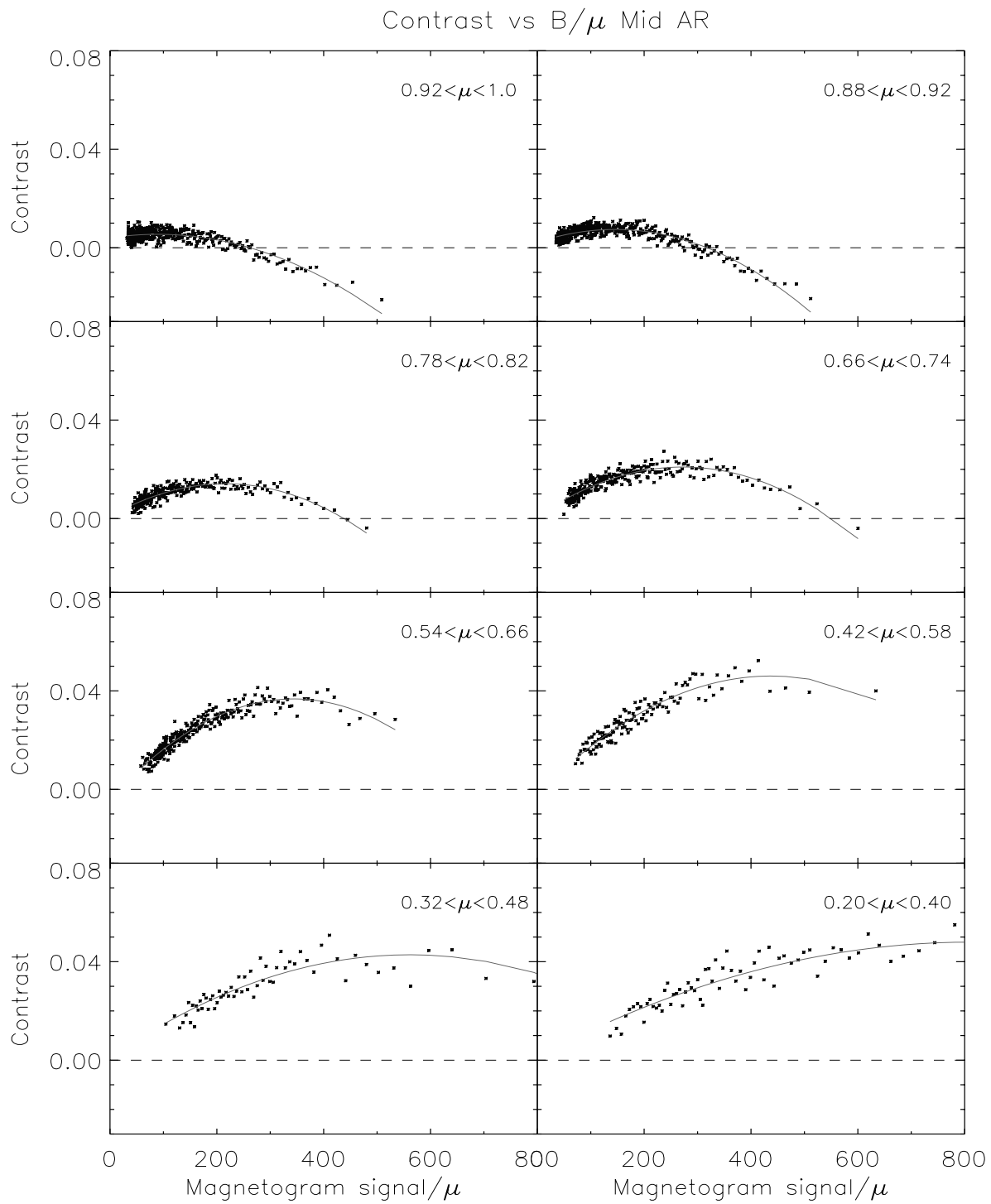


Figure D.10: The same as figure D.7 for the AR component at mid cycle.

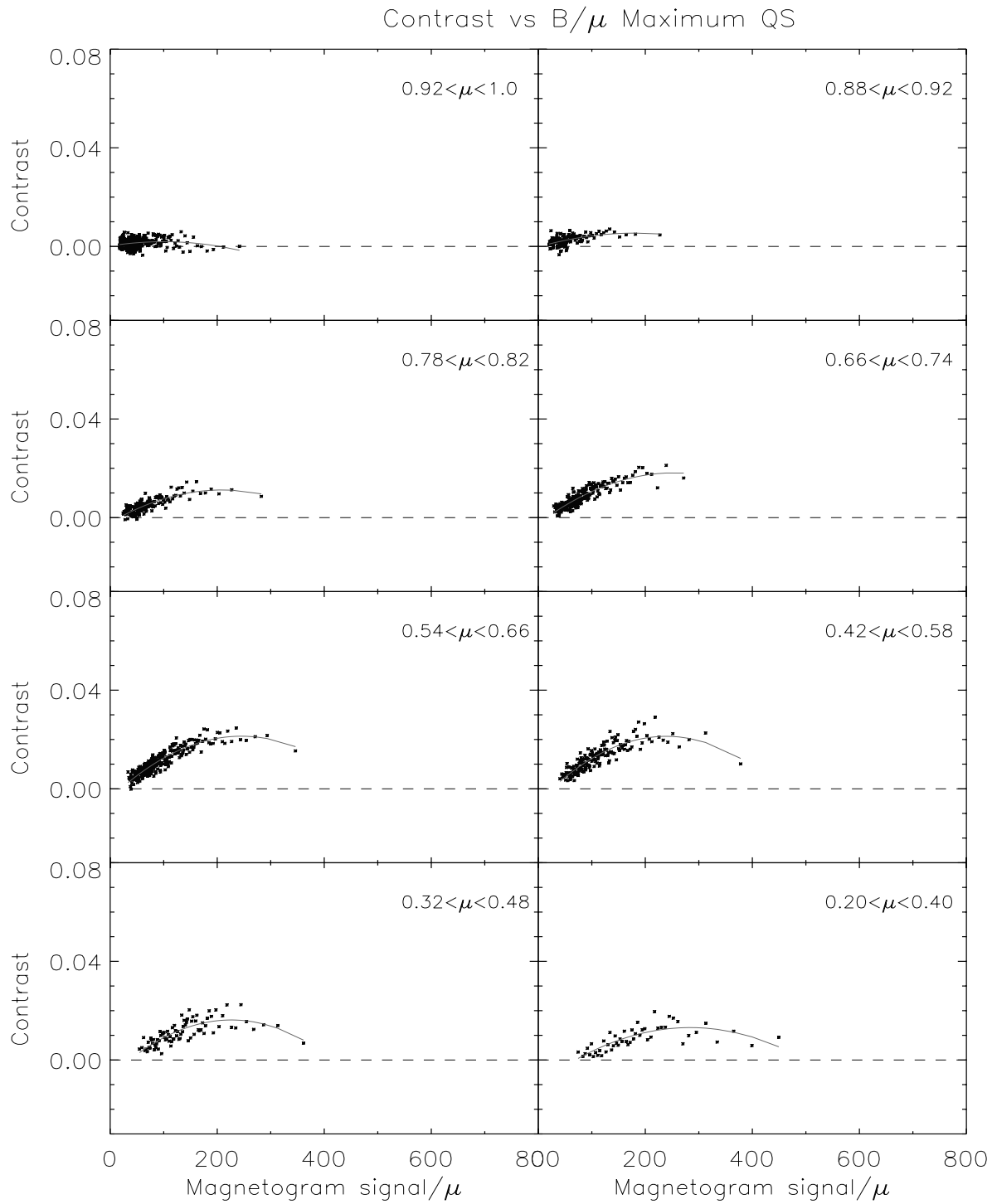


Figure D.11: The same as figure D.7 for the QS component at solar maximum.

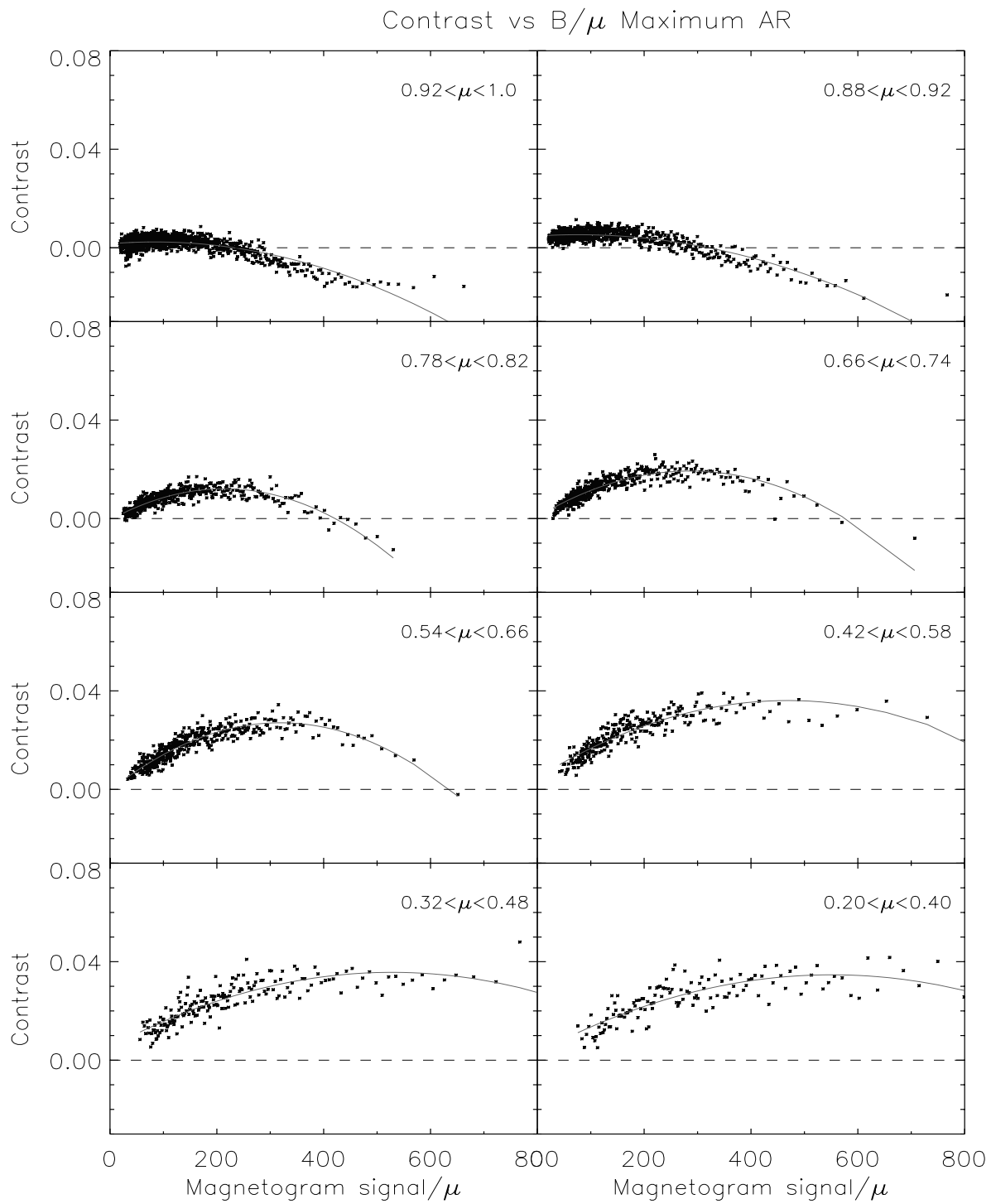


Figure D.12: The same as figure D.7 for the AR component at solar maximum.

